



FIRST-PRINCIPLES STUDY OF GaAs/AlAs NANOWIRE HETEROSTRUCTURES

A THESIS SUBMITTED TO  
THE GRADUATE SCHOOL OF NATURAL AND APPLIED SCIENCES  
OF  
MIDDLE EAST TECHNICAL UNIVERSITY

BY

SELMA ŞENOZAN

IN PARTIAL FULFILLMENT OF THE REQUIREMENTS  
FOR  
THE DEGREE OF DOCTOR OF PHILOSOPHY  
IN  
PHYSICS

AUGUST 2012

Approval of the thesis:

**FIRST-PRINCIPLES STUDY OF GaAs/AlAs NANOWIRE HETEROSTRUCTURES**

submitted by **SELMA ŞENOZAN** in partial fulfillment of the requirements for the degree of **DOCTOR OF PHILOSOPHY** in **Physics Department, Middle East Technical University** by,

Prof. Dr. Canan Özgen \_\_\_\_\_  
Dean, Graduate School of **Natural and Applied Sciences**

Prof. Dr. Mehmet Zeyrek \_\_\_\_\_  
Head of Department, **Physics**

Prof. Dr. Mehmet Tomak \_\_\_\_\_  
Supervisor, **Physics Department, METU**

**Examining Committee Members:**

Prof. Dr. Yakup Cevdet Akgöz \_\_\_\_\_  
Engineering Sciences Dept., METU

Prof. Dr. Mehmet Tomak \_\_\_\_\_  
Physics Dept., METU

Prof. Dr. Mehmet Çakmak \_\_\_\_\_  
Physics Dept., Gazi University

Assoc. Prof. Dr. Sadi Turgut \_\_\_\_\_  
Physics Dept., METU

Assist. Prof. Dr. Hande Toffoli \_\_\_\_\_  
Physics Dept., METU

**Date:** \_\_\_\_\_

**I hereby declare that all information in this document has been obtained and presented in accordance with academic rules and ethical conduct. I also declare that, as required by these rules and conduct, I have fully cited and referenced all material and results that are not original to this work.**

Name, Last Name: SELMA ŞENOZAN

Signature :

# ABSTRACT

## FIRST-PRINCIPLES STUDY OF GaAs/AlAs NANOWIRE HETEROSTRUCTURES

Şenozan, Selma

Ph.D., Department of Physics

Supervisor : Prof. Dr. Mehmet Tomak

August 2012, 66 pages

Nanowire heterostructures play a crucial role in nanoscale electronics, i.e., one-dimensional electronics derives benefits from the growth of heterostructures along the nanowire axis. We use first-principles plane-wave calculations within density functional theory with the localized density approximation (LDA) to get information about the structural and electronic properties of bare and hydrogen passivated GaAs/AlAs nanowire heterostructures. We also take into account the reconstruction of the nanowire surfaces. Modeled nanowire heterostructures are constructed using bulk atomic positions along [001] and [111] direction of zinc-blende structures and cutting out wires from this GaAs/AlAs heterostructure crystal with a diameter of 1 nm. We study for the effects of the surface passivation on the band gap and the band offsets for the planar GaAs/AlAs bulk heterostructure system and GaAs/AlAs nanowire heterostructure system. It is possible to control the potential that carriers feel in semiconductor heterostructures. For the planar lattice-matched heterostructures, the macroscopic average of potential of the two materials is constant far from the interface and there is a discontinuity at the interface depending on the composition of the heterostructure. In order to obtain the valence band offset in the heterostructure system, the shift in the macroscopic potential at the interface and the difference between the valence band maximum values of the two constituents must be added. In nanoscale heterostructures, the potential profile presents a more

complex picture. The results indicate that while the discontinuity remains close to the planar limit right at the interface, there are fluctuations on the average potential profile beyond the interface developed by the inhomogeneous surface termination, that is, there are variations of the band edges beyond the interface.

We report a first-principles study of the electronic properties of surface dangling-bond (SDB) states in hydrogen passivated GaAs/AlAs nanowire heterostructures with a diameter of 1 nm, where the SDB is defined as the defect due to an incomplete passivation of a surface atom. The charge transition levels  $\epsilon(+/-)$  of SDB states serve as a common energy reference level, such that charge transition level  $\epsilon(+/-)$  value for group III and V atoms is a constant value and a periodic table atomic property.

We have carried out first-principles electronic structure and total energy calculations of aluminum nanowires for a series of different diameters ranging from 3Å-10Å, which is cut out from a slab of ideal bulk structure along the [001] direction. First-principles calculations of aluminum nanowires have been carried out within the density-functional theory. We use the norm-conserving pseudopotentials that are shown to yield successful results for ultrathin nanowire regime. Our results show that the number of bands crossing the Fermi level decreases with decreasing wire diameter and all wires studied are metallic.

Keywords: Nanowire heterostructure, density functional theory, first-principles, band offset, surface passivation

# ÖZ

## GaAs/AlAs NANOTEL HETEROJEN YAPILARDA İLK-PRENSİPLER HESABI

Şenozan, Selma

Doktora, Fizik Bölümü

Tez Yöneticisi : Prof. Dr. Mehmet Tomak

Ağustos 2012, 66 sayfa

Nanotel heterojen yapılar nano ölçek elektroniğinde önemli bir rol üstlenir. Diğer bir deyişle, tek boyutlu elektronikte heterojen yapıların nanotel ekseni boyunca büyümesinden faydalanılır. Saf ve yüzeyi hidrojen ile pasifleştirilmiş GaAs/AlAs nanotel heterojen yapılarının yapısal ve elektronik özelliklerini elde etmek için yoğunluk fonksiyoneli teorisi içindeki ilk-prensipier düzlem dalga hesaplamalarını yerleştirilmiş yoğunluk yaklaşımı (LDA) ile birlikte kullandık. Ayrıca nanotel yüzeylerinin yeniden yapılandırılmasını da dikkate aldık. Modellenmiş nanotel heterojen yapılar çinkoblend yapıların [001] ve [111] doğrultusundaki kristal atomik pozisyonları kullanılarak ve bu GaAs/AlAs heterojen yapı kristalinden 1nm çapında teller kesip çıkarılarak inşa edilmiştir. Yüzey pasifleştirilmesinin GaAs/AlAs nanotel heterojen yapı sisteminin bant boşluğu ve bant süreksizliği üzerindeki etkileri üzerine çalıştık. Taşıyıcıların yarı iletken heterojen yapılar içinde hissettiği potansiyeli kontrol etmek mümkündür. Kristal heterojen yapılar için, iki malzemenin potansiyellerinin makroskopik ortalama değeri arayüzden uzakta sabittir, heterojen yapının bileşimine bağlı olarak arayüzde bir süreksizlik vardır. Heterojen yapı sistemindeki değerlilik bant kaymasını elde etmek için arayüzde varolan makroskopik potansiyeldeki kayma ve iki bileşenin değerlilik bantı maksimum değerleri arasındaki fark eklenmelidir. Nano ölçekli heterojen yapılarda, potansiyel profili daha karmaşık bir resim oluşturur. Sonuçlar göstermektedir ki, süreksizlik tam arayüzde düzlemsel limite yakın kalırken,

arayüzün ötesinde oluşan ortalama potansiyelde homojen olmayan yüzey pasifleştirilmesinden kaynaklanan dalgalanmalar oluşmaktadır, yani arayüzün ötesinde bant uç değerlerinde değişimler vardır.

Yarıçapı 1 nm olan ve yüzeyi hidrojen ile pasifleştirilmiş GaAs/AlAs nanotel heterojen yapılarında yüzey üzerinde hidrojen ile bağ yapmamış tek bir atom kusur olarak bırakılarak yüzey bağ durumları için ilk prensipler çalışması yapılmıştır. III ve V grubundaki atomlar için yük transfer seviyeleri  $\epsilon(+/-)$  sabit olduğu ve bir periyodik tablo özelliği olduğu için bu yüzey bağ durumlarının yük transfer seviyeleri  $\epsilon(+/-)$  ortak bir enerji seviyesi olarak düşünülebilir.

Yarıçapı 3 Å ile 10 Å arasında değişecek şekilde [001] doğrultusundaki kristal yapıdan kesilerek inşa edilmiş alüminyum nanotel yapılar için ilk prensipler elektronik yapı ve toplam enerji hesapları yapılmıştır. Bu alüminyum nanoteller için yapılan ilk prensipler hesaplamaları yoğunluk fonksiyonel teorisine dayanmaktadır. Çok ince nanotellerde başarılı sonuçlar sağladığı için norm koruyucu pseudo-potansiyel kullanılmıştır. Sonuçlarımız Fermi seviyesini kesen bant sayısının telin yarıçapı azaldıkça azaldığını ve çalıştığımız tüm nanotellerin metallik yapıda olduğunu göstermiştir.

Anahtar Kelimeler: Nano tel heterojen yapılar, yoğunluk fonksiyonel teorisi, ilk prensipler, bant süreksizliği, yüzey pasifleştirilmesi



*To my big family*

## ACKNOWLEDGMENTS

First, I would like to express my sincere appreciation to my thesis advisor Prof. Mehmet Tomak for his guidance and support during my study and the freedom that I was granted in organizing the research and time. He always responded to all of my questions with the utmost patience.

I am very grateful to Assist. Prof. Dr. Hande Toffoli for introducing me into this stirring research field of *ab initio* calculations and for being such an important guide in this work. She has supported this study patiently, through her stimulating suggestions.

I am strongly indebted to Soner Bař, who has helped me in every aspect of my thesis and my life. This work could not have been completed without the presence of him and my pets Köpük, Sabun and Zappa. They are “my big family“. Also many many thanks to Sadiye and Zübeyde Bilge Bař for all the delicious dinners and Yener Bař for his kind support.

Special thanks to Nazım Dugan, the first person helping me about the installing and configuring the Quantum Espresso. And to my friend Dr. Emre Sururi Tařçı for bringing his good spirit to METU and to Turan Birol for invaluable discussions. I owe infinitely many thanks to my friend Kıvanç Uyanık for thousands of coffees, lunches and discussions together. Thanks to Ceren Sibel Sayın for her patience in answering my research related questions and for further discussions. During all these years of study there are people who changed my life, Duygu Can, Kerem Altun, Esra and Ayhan Ayatar are those people, many many thanks for being a part my life, your friendships are priceless.

I am very grateful to Prof. Mustafa Savcı for accepting me as a friend and as a colleague. His presence and support during the daily ups and downs were very appreciated. Moreover, I do not want to forget a lot of people, with whom I shared a good time at METU: Meral Bozkurt, Kıvılcım Bařak Vural, Mehmet Ali Olpak, Ece Ařılar, Gökhan Alkaç, Özge Bayraklı, Merve Demirtař, Deniz Olgu Devociođlu, Selçuk Bilmiř, Özge Tozkar, Mert Elverici.

I would like to thank also The Scientific and Technological Research Council of Turkey

(TUBITAK). All the numerical calculations presented in this thesis have been performed at TUBITAK ULAKBIM, High Performance and Grid Computing Center (TR-Grid) and my thesis was partially supported by the 2211-TUBITAK PhD. Scholarship Programme.

Finally, I thank to my mother, my father and my brothers for their endless love and support during my long years of study.

# TABLE OF CONTENTS

ABSTRACT . . . . .	iv
ÖZ . . . . .	vi
ACKNOWLEDGMENTS . . . . .	ix
TABLE OF CONTENTS . . . . .	xi
LIST OF TABLES . . . . .	xiii
LIST OF FIGURES . . . . .	xiv
CHAPTERS	
1 INTRODUCTION . . . . .	1
1.1 Computational approach . . . . .	3
1.2 Modelling heterostructures with supercells . . . . .	6
1.3 Band Line-ups . . . . .	6
2 THEORETICAL BACKGROUND . . . . .	10
2.1 Adiabatic Approximation . . . . .	11
2.2 Pre-Density Functional Theory . . . . .	11
2.2.1 Hartree and Hartree-Fock approximation . . . . .	11
2.2.2 Thomas-Fermi Theory . . . . .	13
2.3 Modern Density Functional Theory . . . . .	13
2.3.1 Hohenberg-Kohn Theory . . . . .	13
2.3.2 The Kohn-Sham equations . . . . .	14
2.4 Functionals for Exchange and Correlation . . . . .	15
2.4.1 The Localized Density Approximation (LDA) . . . . .	15
2.4.2 Generalized Gradient Approximation (GGA) . . . . .	16
2.5 Plane-wave Basis Set for Kohn-Sham Orbitals . . . . .	16
2.5.1 Bloch's Theorem . . . . .	16

	2.5.2	k-point Sampling . . . . .	17
	2.5.3	Plane-wave Representation of Kohn-Sham Equations . . . . .	17
	2.6	Pseudopotentials . . . . .	18
3		GaAs/AlAs BULK HETEROSTRUCTURE SYSTEM . . . . .	20
	3.1	Method . . . . .	20
	3.2	Bulk properties of GaAs and AlAs . . . . .	21
	3.3	GaAs/AlAs(001) heterostructure . . . . .	23
	3.4	Theoretical study of band-offsets at the interface . . . . .	24
4		GaAs/AlAs NANOWIRE HETEROSTRUCTURE SYSTEM . . . . .	27
	4.1	Method . . . . .	27
	4.2	GaAs and AlAs nanowires . . . . .	28
	4.3	Modelling GaAs/AlAs Nanowire Heterostructure System with Supercell . . . . .	35
	4.4	Bare and H-passivated GaAs/AlAs Nanowire Heterostructures . . . . .	35
	4.4.1	Atomic Structure and Energetics . . . . .	37
	4.4.2	Band Structure and Band Offset of GaAs/AlAs Nanowire Heterostructures . . . . .	41
	4.5	Surface dangling-bond states in H-passivated GaAs/AlAs NWHETs . . . . .	47
	4.6	Summary . . . . .	50
5		ALUMINUM NANOWIRES . . . . .	51
	5.1	Method and Atomic Structure . . . . .	53
	5.2	Results and Discussions . . . . .	53
	5.3	Summary . . . . .	55
6		CONCLUSION . . . . .	59
		REFERENCES . . . . .	62
		VITA . . . . .	65

## LIST OF TABLES

### TABLES

Table 3.1	Lattice parameters for GaAs and AlAs . . . . .	22
Table 3.2	Valence band maximum and band gap for GaAs and AlAs . . . . .	23
Table 4.1	The lattice constant $a_0$ and the cohesive energy per Ga-As (Al-As) atom pair values for GaAs (AlAs) nanowires in the [111] direction, using Eq. 4.1 and Eq. 4.2	34
Table 4.2	The binding energy of hydrogen for GaAs (AlAs) nanowires in the [111] direction with respect to the free H atom, using Eq. 4.3 . . . . .	34
Table 5.1	Aluminum nanowire lattice constant along the wire axis. . . . .	54
Table 5.2	Cohesive energy per Al atom pair $E_c$ of different radius Al nanowires calculated using Eq. (1). . . . .	56

# LIST OF FIGURES

## FIGURES

Figure 1.1 The geometry of the H-terminated GaAs/AlAs nanowire heterostructure along the [111] direction and side views. . . . .	4
Figure 1.2 GaAs/AlAs NWHET supercell, with axis oriented along the [111] direction, in the x-y plane and slightly off-axis are shown. Ga, Al, As and H atoms are represented by purple, dark blue, yellow and light blue circles, respectively. . . . .	5
Figure 1.3 GaAs/AlAs heterostructure interface, straddling lineup. . . . .	6
Figure 1.4 $(GaAs)_3(AlAs)_3$ along [001] direction, where the interface is simulated by a 6+6 superlattice where Ga, Al, As atoms are represented by purple, dark blue and yellow circles, respectively. . . . .	8
Figure 3.1 Equilibrium lattice constant of GaAs and AlAs. . . . .	21
Figure 3.2 AlAs band structure and DOS . . . . .	22
Figure 3.3 GaAs band structure and DOS . . . . .	22
Figure 3.4 $(GaAs)_3(AlAs)_3$ oriented along the direction (100) interface simulated by a 6+6 superlattice where Ga, Al, As atoms are shown by purple, dark blue and yellow circles, respectively. . . . .	23
Figure 3.5 For $(GaAs)_3(AlAs)_3$ superlattices the planar average and macroscopic average of electrostatic potential along the growth direction is shown, respectively. $\Delta V$ corresponds to the difference between the plateaus, which is 0.54 eV in here. . . . .	26
Figure 4.1 Relaxed bare GaAs nanowire oriented along the [001] direction: GaAsNW(42), where Ga and As atoms are shown by purple and yellow circles, respectively. . . . .	29
Figure 4.2 H-passivated GaAs nanowire oriented along the [001] direction: H-GaAsNW(82), where Ga, As, and H atoms are represented by purple, yellow and light blue circles, respectively. . . . .	29

Figure 4.3 Relaxed bare GaAs nanowire oriented along the [111] direction: GaAsNW(38), where Ga and As atoms are represented by purple and yellow circles, respectively. . . . .	30
Figure 4.4 H-passivated GaAs nanowire oriented along the [111] direction: H-GaAsNW(68), where Ga, As, and H atoms are represented by purple, yellow and light blue circles, respectively. . . . .	30
Figure 4.5 AlAs NW(38) along [111] direction and side views, where Al and As atoms are represented by dark blue and yellow circles, respectively. The surface reconstruction along this direction is in the second line. . . . .	31
Figure 4.6 H-passivated AlAs nanowire oriented along the [111] direction: H-AlAsNW(68), where Al, As, and H atoms are represented by dark blue, yellow and light blue circles, respectively. . . . .	31
Figure 4.7 Band structures of GaAsNW(38) and H-GaAsNW(68) in [111] direction with surface dangling bonds not passivated and passivated with hydrogenlike pseudoatoms, respectively. The surface states are removed from the band gap when the surface dangling bonds have been passivated. . . . .	32
Figure 4.8 Band structures of AlAsNW(38) and H-AlAsNW(68) in [111] direction with surface dangling bonds not passivated and passivated with hydrogenlike pseudoatoms, respectively. The surface states are removed from the band gap when the surface dangling bonds have been passivated. . . . .	33
Figure 4.9 GaAs/AlAs NWHET supercell in the x-y plane and slightly off-axis where Ga, Al, As atoms are represented by purple, dark blue and yellow circles, respectively. . . . . .	36
Figure 4.10 Surface reconstruction of GaAs/AlAs NWHET along [001] direction. Ga, Al, As atoms are represented by purple, dark blue and yellow circles, respectively. . . . .	38
Figure 4.11 Charge density contour plots of reconstructed GaAs/AlAs NWHET along [001] direction, lateral plane is shown in left panel and vertical plane is in right plane. . . . .	38
Figure 4.12 GaAs/AlAs NWHET(76) along [111] direction and side views. The surface reconstruction along this direction is in the second line. . . . .	39
Figure 4.13 When $Z=0.5$ the pseudohydrogen bond in the cations are broken, when $Z=1$ the hydrogen bond in the cation atoms are broken. . . . .	39



Figure 4.14 Relaxed GaAs/AlAs NWHET(82) oriented along the [001] crystallographic direction with the termination of dangling bonds with H-atom. Ga, Al, As, H atoms are represented by purple, dark blue, yellow and light blue circles, respectively. The relaxed structure is in the second line is when H* (Z=1.25) and H* (Z=0.75) for cations and anions, respectively. . . . .	40
Figure 4.15 H-GaAs/AlAs NWHET(136) along [111] direction and side views of it with the termination of dangling bonds by H-atom and in the second line the relaxed coordinates are shown when H* (Z=1.25) and H* (Z=0.75) for cations and anions, respectively. . . . .	40
Figure 4.16 Band structures of GaAs/AlAs NWHET(42) and H-GaAs/AlAs NWHET(82) in [001] direction with surface dangling bonds not passivated and passivated with hydrogenlike pseudoatoms, respectively. The surface states are removed from the band gap when the surface dangling bonds have been passivated. . . . .	42
Figure 4.17 Band structures of GaAs/AlAs NWHET(76) and H-GaAs/AlAs NWHET(136) in [111] direction with surface dangling bonds not passivated and passivated with hydrogenlike pseudoatoms, respectively. The surface states are removed from the band gap when the surface dangling bonds have been passivated. . . . .	43
Figure 4.18 For $(GaAs)_3(AlAs)_3$ superlattices the planar average (dotted line) and macroscopic average (solid line) of electrostatic potential along the growth direction are shown, a steplike behavior is seen. The potential shift corresponds to the difference between the plateaus, which is 0.54 eV in here. . . . .	45
Figure 4.19 The planar (dotted line) and macroscopic (solid line) average of electrostatic potential for the GaAs/AlAs NWHET in the [111] direction with different number of atom supercells, i.e. alternating slabs of GaAs and AlAs are increased. The potential profile for 3+3 and 6+6 superlattice are shown, respectively. . . . .	46
Figure 4.20 Band structures of AlAs and GaAs nanowires with one surface dangling-bond defect, on the left and right side, respectively. Orientation of the wires are along the [111] direction. . . . .	49
Figure 5.1 Top and side views of aluminum nanowires with radius (a) $3\text{\AA}$ (4), (b) $5\text{\AA}$ (16), (c) $7\text{\AA}$ (32) and (d) $10\text{\AA}$ (76). . . . .	54

Figure 5.2 Band structures of Al nanowires with radius (a) $3\text{\AA}$ (4), (b) $5\text{\AA}$ (16), (c) $7\text{\AA}$ (32) and (d) $10\text{\AA}$ (76) . . . . .	56
Figure 5.3 Charge density contour plots in lateral and vertical planes are shown in left panels and right panels, respectively. (a) and (b): $3\text{\AA}$ (4). (c) and (d): $5\text{\AA}$ (16). (e) and (f): $7\text{\AA}$ (32). (g) and (h): $10\text{\AA}$ (76). . . . .	57

# CHAPTER 1

## INTRODUCTION

Semiconductor nanowires have great potential for technological implementations, i.e. with periodicity in one dimension and charge carrier confinement in two directions nanowires are quasi-one-dimensional systems also with a large surface/volume ratio and a small cross-section area. For particular applications, the chosen nanowire system is conducted by the information about the efficiency of the corresponding bulk materials. Nanowires have the advantage that many of their properties can be managed by adjusting diameter, growth direction, structural phases, and the faceting or surface saturation, that is, during the growth process it is possible to control the electronic structure of the nanowire. The recent improvements in catalytic growth of semiconductor nanowires lead the way to synthesize high-quality heterostructures with distinguished transport and optical properties. The nanowire composition can be modulated along the growth direction and along the radial direction, which are called axial heterostructures and core-shell structures, respectively. Resonant tunneling diodes [1], nanoscale field effect transistors [2], Coulomb blockade devices [3, 4, 5], and quantum dot memories [6, 7] are examples of nanowire heterostructure (NWHET) based devices.

There are numerous recent study of electronic structure calculations of semiconductor nanowire superlattices including GaAs/AlGaAs [8], Ge/Si [9]. Persson *et al.* [8] studied the electronic structure of GaAs/AlGaAs nanowires, such as energy gap opening and miniband formation and showed that the proper passivation of the surface by hydrogenlike pseudoatoms is important to clean the band gap from the surface states. Niquet *et al.* [10] computed band offsets in core/shell and axial GaAs/AlAs nanowire superlattices with radius 5 nm and 75000 atoms, using self-consistent tight-binding calculations and found that for the nanoscale heterostructures, the band discontinuity at the interface is nearly independent of the size and shape, but the band edges not exactly behaving like a step function beyond the interface as in the planar

case. They stated that the universally accepted picture for the potential behavior in planar lattice-matched heterostructures, which is constant away from the interface and there is a step at the interface, could be invalid in nanoscale heterostructure. Their results indicated that the band edges shows important oscillations away from the interfaces unless the nano-structures are surrounded with a shell which is homogeneous, that is, in axial nanowire heterostructures the band edges have a more complicated manner depending on the nature of the surfaces. They have also computed the band offset of nanowires with an external AlAs shell and illustrated the necessity of the surface termination, such that, with this AlAs shell the valence band edge is constant everywhere except at the interface. In an experimental study Xiaocheng *et al.*[11] reported the growth of InAs/InP radial core/shell nanowire heterostructures in which the InAs surfaces were passivated with 1 nm thick InP shell to create a cylindrical quantum well populated with nanowire heterostructure motif. They have stated that, InP is chosen as a capping material since the conduction band offset value of InP creates a confinement potential for electrons. A recent experiment [12] have shown that engineering of the nanocrystals surface capping would allow tuning of energy levels alignment. However, very little theoretical research has been done for the band-offset in nanosize heterostructure systems. Leonard and Tersoff [13] found that when a semiconductor carbon nanotube is contacted to a metal, the Schottky barrier height can't be fixed by Fermi level pinning as in semiconductor-metal junctions, that is, the behavior is completely different in nanoscale. The summary of finding up to now is that, applications of the concepts of band offsets, driven from the planar heterostructure systems, to nanoscale heterostructure systems is debatable.[10, 13] There are also numerous recent study of electronic structure calculations of semiconductor nanowires including Si, [14, 15, 16, 17, 18] ZnO, [19] GaAs, [20]. Zheng *et al.* [16] stated that the band gap of hydrogen passivated Si nanowires increases with decreasing diameter. Rurali *et al.* [18] studied the relation between the reconstruction of Si [100] nanowire surfaces and transport properties of the Si [100] nanowires and they stated that due to the reconstruction it is possible for the surface state in the band gap to cross the Fermi level. Cahangirov *et al.* [20] computed six different types of GaAs nanowires with different diameters along [111] direction and investigated the cohesive energy, band gap and hydrogen passivation of surface dangling bonds using first-principles pseudopotential calculations using ultrasoft pseudopotentials.[21]

The purpose of this thesis, is to make an extensive analysis of GaAs/AlAs nanowire heterostructures for further studies in addition to experimental and theoretical studies of pla-

nar heterostructure systems. To this end, we undertake a first-principles study on electronic and structural properties of GaAs/AlAs nanowire heterostructures grown along the [111] and [001] directions. We have examined in which way the hydrogen saturation of dangling bonds of surface atoms affects the electronic structure of the nanowire. Also the possible surface reconstruction is taken into account through relaxation. The potential profile of GaAs/AlAs NWHET system is determined by the surface passivation in addition to the discontinuity at the interface. This is because the potential along the axis of the NWHET system depends both on the dipole layer at each interface and at the surface of the NWHET system. NWHET systems require more detailed treatment relating their symmetry, dimensionality and surface passivation. The results indicate that while the discontinuity remains close to the planar limit right at the interface, there are fluctuations on the potential profile beyond the interface.

In this thesis, we make an investigation of the electronic structure of the GaAs/AlAs nanowire heterostructures and the effect of dangling bond passivation on the electronic structure using first-principles density functional theory calculations. In the first chapter there is an introduction part, after that in the second chapter Density Functional theory is briefly mentioned. First-principles study of GaAs/AlAs heterostructures (HETs) is in Chapter 3 and first-principles study of GaAs/AlAs nanowire heterostructures (NWHETs) and results is in Chapter 4. In Chapter 5, electronic properties of aluminum nanowires are discussed as an example of a metallic nanowire.

## 1.1 Computational approach

The fundamental improvement in the application of *ab initio* approaches to material science began with the Density Functional Theory (DFT) in 1960. Kohn has proposed that many electron system's total energy is a functional of the electron density distribution. After that, the interacting electrons in the many body problem has been reduced to a system of single-particle Kohn-Sham equations, which are solved iteratively and self-consistently. The usage of DFT in real systems can be possible by the application of approximations for the exchange-correlation functional. Local density approximation (LDA) is one of the exchange-correlation functional, which has proven to give reliable results on the ground-state properties of crystals at an acceptable computational burden. Exchange-correlation functional in the LDA is a function of the local charge density. Generalized gradient approximation (GGA) is another

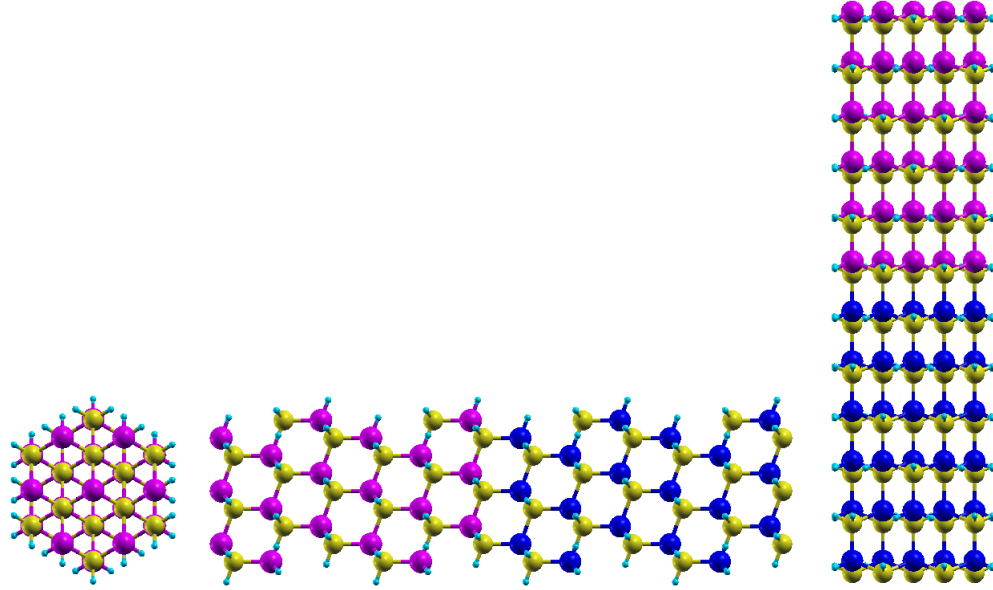


Figure 1.1: The geometry of the H-terminated GaAs/AlAs nanowire heterostructure along the [111] direction and side views.

approximation for the exchange-correlation functional which takes into account the gradient of the charge density distribution.

For the heterostructure system, the study of interface has been accomplished using the pseudopotential method, in which only the valence electrons are treated and the core electrons is substituted by almost smooth pseudopotentials. For periodic solids Kohn-Sham electronic orbitals are expanded with a plane wave basis set which is up to an energy cutoff value. Integrals over the Brillouin zone are performed by a discrete summation over a special set of  $\mathbf{k}$ -points. The discretization of the  $\mathbf{k}$ -points is another approximation. In this thesis, we have used Monkhorst-Pack scheme to cover the Brillouin zone with a uniform grid. Numerical accuracy of electronic calculations are determined by the choice of  $\mathbf{k}$ -point mesh and energy cutoff. Generally, the sources of errors are the choice of the pseudopotentials and the exchange-correlation functional approximations. It is essential to undertake convergence tests for the materials constituting the heterostructure system in order to ensure the accuracy of the results. The PWSCF code is used to study of heterostructure[22].

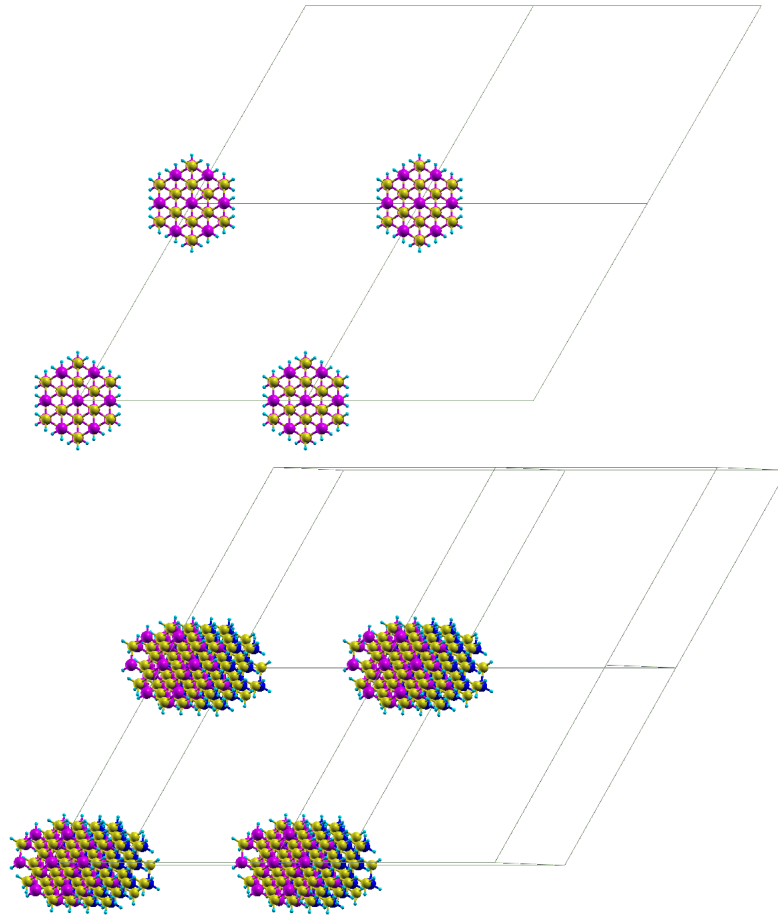


Figure 1.2: GaAs/AlAs NWHET supercell, with axis oriented along the [111] direction, in the x-y plane and slightly off-axis are shown. Ga, Al, As and H atoms are represented by purple, dark blue, yellow and light blue circles, respectively.

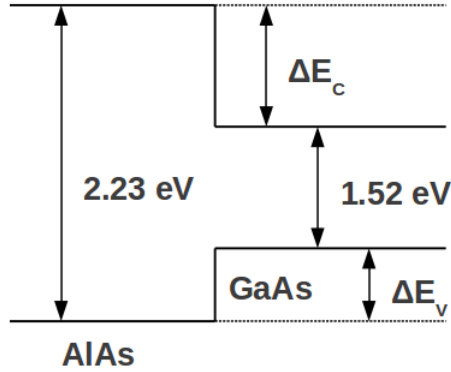


Figure 1.3: GaAs/AlAs heterostructure interface, straddling lineup.

## 1.2 Modelling heterostructures with supercells

Periodically repeated supercells are used in order to study heterostructures to eliminate the loss of translational symmetry. The changes made by an interface are only in a small region. The interface characteristics can be studied using supercells with a couple of atomic layers of each material.

All nanowires studied here are constructed by selecting an axis along a crystallographic direction in bulk zinc blende and taking the atoms which are in a chosen distance from the nanowire axis. Besides GaAs and AlAs nanowires we also consider a nanowire with a periodic repetition of a couple of GaAs and AlAs planes, constituting a GaAs/AlAs nanowire heterostructure. The geometry is shown in Fig. 1.1, constructed by the repetition of three layers of GaAs and three layers of AlAs. The H-terminated nanowires are obtained by saturating the surface dangling with hydrogen. For all nanowire structures the lattice parameter and atomic positions were relaxed. In Fig. 1.2 the supercell for GaAs/AlAs nanowire heterostructure system in the  $x$ - $y$  plane and slightly off-axis is shown.

## 1.3 Band Line-ups

When two semiconductors with different band gaps are brought into contact at an interface, their band edges will align. The interface formed by III-V compounds are like in Fig. 1.3. In such an interface, there is a charge flow from the larger gap semiconductor to the smaller gap semiconductor, creating a potential barrier.



Interface band offset can be calculated using first-principle calculations. The band structures of the two individual materials is not sufficient to determine the band offset, the potential line-up across the interface is also needed. The determination of band offsets at interfaces of heterostructures is a necessity for semiconductor device design since by controlling the band offsets we can control the confinement and the carrier flow.

Band offsets have been calculated using moderately refined methods at the interfaces of heterostructures. First methods depended on obtaining one bulk-specific parameter, that had been used to obtain the offset. Anderson affinity rule [23] and effective midgap state theory of Tersoff [24] are the most important methods in determining the lineup without using any information about the interface. A straightforward but inconvenient method could be calculating the complete heterostructure and searching for the local density of states [25]. Afterwards, methods that integrate information from the two separate bulk calculations and from the interface calculation have become popular [26, 27, 28, 29, 30, 31], which can be feasible for *ab-initio* computational calculations. Together with the vast amounts of computational utilities, calculating the band line-ups from first-principle calculations has become possible for the heterostructure systems [28, 29, 30, 32].

Baldereschi *et al.* [30] have calculated the xy planar averaged potential by taking the average in the growth direction to get a curve for the potential which is varying slowly, from where potential shifts have been obtained. From a heterostructure calculation estimating the change in the average electrostatic potential through the interface and then aligning the bulk valence-band maximum (VBM) of two semiconductor constituents according to this average electrostatic potential will give us the valence-band offset (VBO). We will use the average electrostatic potential technique [30] to get the valence-band offset in  $(GaAs)_3(AlAs)_3$  superlattices oriented in (001) direction.

Our calculations are performed on a superlattice geometry. The interface characteristics are studied using a few atomic planes of each GaAs and AlAs materials. Supercells contain two interfaces, so we get the isolated interface configuration by making the adjacent interfaces separated from each other. The 6+6 superlattice is shown in Fig. 1.4, here GaAs/AlAs interface has been simulated by a 6+6 superlattice and from the self-consistent calculations we get the charge density and electrostatic potential. Since planes parallel to the interface are periodic we have obtained planar averages of charge density and electrostatic potential as

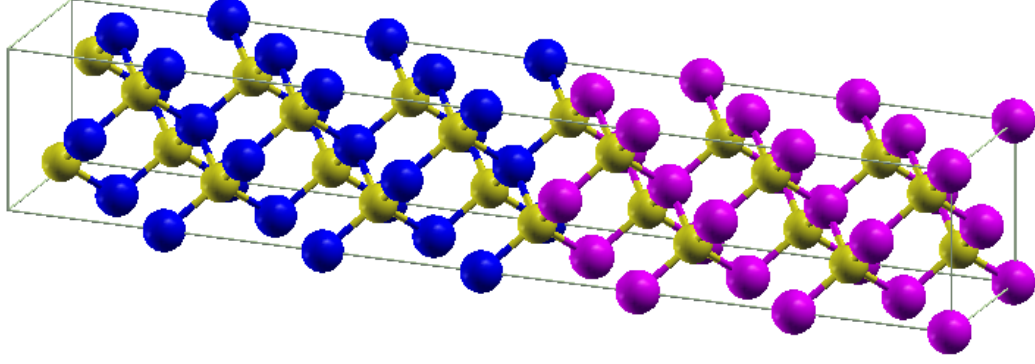


Figure 1.4:  $(GaAs)_3(AlAs)_3$  along [001] direction, where the interface is simulated by a 6+6 superlattice where Ga, Al, As atoms are represented by purple, dark blue and yellow circles, respectively.

a function of the direction perpendicular to the interface, which is  $z$  coordinate, the growth direction:

$$\bar{f}(z) = \frac{1}{S} \int_S f(x, y, z) dx dy \quad (1.1)$$

If we look at the plot of these planar averages of  $\bar{\rho}(z)$  and  $\bar{V}(z)$  we get periodic functions in GaAs and AlAs materials, smoothly joining across the interface. For the GaAs/AlAs HET system, which is a lattice-matched one, on each side of the interface the period of these periodic functions of  $\bar{\rho}(z)$  and  $\bar{V}(z)$  are the same, which is the half of the bulk lattice parameter. There is a slight difference between these periodic functions due to the effect of the interface which could be enhanced by excluding the bulk-like variations using the macroscopic average technique, which is the one dimensional average of  $\bar{f}$  over a period centered at  $z$ :

$$\bar{\bar{f}}(z) = \frac{1}{\alpha} \int_{z-\alpha/2}^{z+\alpha/2} \bar{f}(z') dz' \quad (1.2)$$

There is no oscillation on the two part of the interface for the macroscopically averaged quantities, and we get a constant limit in each part of the heterostructure. In the interface region deviations are seen from this macroscopic limit. The potential shift can be obtained from this slowly varying curve. The results about planar band line-ups in GaAs/AlAs HET system are presented in Chapter 3.

For nanowire superlattices, which consists of successive segments of GaAs and AlAs nanowires, the potential profile is determined by the surface passivation in addition to the discontinuity at the interface. The potential along the axis of nanowire heterostructure depends both on the dipole layer at each GaAs/AlAs NWHET interface and at the surface of the nanowire. The results indicate that nanoscale heterostructures require more detailed treatments relating their symmetry, dimensionality and surface passivation. The potential shows the same discontinuity right at the interface also in nanoscale, which is connected to the alignment of the charge-neutrality levels[33, 34] on the different sides of the interface. Therefore, the band offset notion is strong for heterostructures in nanoscale, but the potential lineup is not in a step-like behavior as in the planar bulk heterostructures. The results about the band line-ups in hydrogen terminated GaAs/AlAs NWHETs are presented in Chapter 4.

Defining the valence band offset with energies of valence band edges on both sides of the heterostructure is possible, which can be done by defining a common energy level as a reference for both sides of the heterostructure. The reference level approach is made up of assuming that common energy reference is the same on both side of the interface. Theoretically, lots of such common energy level methods have been suggested. Tersoff's theory of effective midgap states [24] predict band lineups with an error of 0.2 eV. Van de Walle *et al.* [35] established an important correlation between the location of hydrogen  $\epsilon(+/-)$  level, which is the Fermi level position where the negative and positive charge states have the same energies, and the band structures of the corresponding material. Kagimura *et al.* [36] found that the charge transition levels  $\epsilon(+/-)$  of SDB states serve like a common energy reference level among Si and Ge wires and Ge/Si heterostructures and they have used this level to predict band line-ups in nanowire heterostructures. In Section 4.5, we report a first-principles calculations for the electronic properties of surface dangling-bond (SDB) states in H passivated GaAs/AlAs NWHETs with a diameter of 1 nm. The SDB is defined as the defect due to an non-passivated surface atom.

## CHAPTER 2

### THEORETICAL BACKGROUND

In this chapter, the theoretical approximations and approaches used in Density Functional Theory (DFT) methods will be presented.

The description of the physical and chemical properties of matter is a many body problem. However, many body systems could be defined as a set of electrons and nuclei interacting through Coulombic forces. It is possible to get the properties of such systems by solving the time-independent Schrodinger equation:

$$H\Psi(\mathbf{r}_i, \mathbf{R}_I) = \varepsilon_i\Psi(\mathbf{r}_i, \mathbf{R}_I) \quad (2.1)$$

where  $\varepsilon_i$  are energy eigenvalues and  $\Psi(\mathbf{r}_i, \mathbf{R}_I)$  are the eigenstates corresponding to these energy eigenvalues.

We can write the Hamiltonian of a many body system in a general form:

$$H = H_{el} + H_{nucl} \quad (2.2)$$

where

$$H_{el} = -\sum_{i=1}^{N_e} \frac{\hbar^2}{2m} \nabla_i^2 + \frac{e^2}{2} \sum_{i=1}^{N_e} \sum_{j \neq i}^{N_e} \frac{1}{|\mathbf{r}_i - \mathbf{r}_j|} - e^2 \sum_{I=1}^{N_n} \sum_{i=1}^{N_e} \frac{Z_I}{|\mathbf{R}_I - \mathbf{r}_i|} \quad (2.3)$$

$$H_{nucl} = -\sum_{I=1}^{N_n} \frac{\hbar^2}{2M_I} \nabla_I^2 + \frac{e^2}{2} \sum_{I=1}^{N_n} \sum_{J \neq I}^{N_n} \frac{Z_I Z_J}{|\mathbf{R}_I - \mathbf{R}_J|} \quad (2.4)$$

where electron coordinates are represented by  $\mathbf{r} = \mathbf{r}_i, i = 1, \dots, N_e$ , and nuclear coordinates are represented by  $\mathbf{R} = \mathbf{R}_I, I = 1, \dots, N_n$ .

$$H = T + V_{ext} + V_{int} + T_I + E_{IJ} \quad (2.5)$$

Obtaining exact solutions for large systems is an impossible task since there are  $3N_e + 3N_n$  degrees of freedom and decoupling of Schrödinger equation is not possible. Therefore, we have to use some approximation methods.

## 2.1 Adiabatic Approximation

To simplify the Schrödinger equation we can use the large mass difference between electrons and nuclei. Hence, electrons move much faster than the nuclei. Therefore, we can assume that electrons are moving in such a field that the nuclei is fixed. This assumption is called Born-Oppenheimer approximation[37]. This allows the factorization of the wave function into nuclear and electronic components. Due to large mass of nuclei, the corresponding kinetic energy can be ignored and the nucleus-nucleus interaction is constant. Assuming these approximations, we only have to solve the many-body electronic Schrödinger equation for the electronic wave function  $\Psi_e(\mathbf{r}_i)$  and for fixed nuclear positions using the Hamiltonian:

$$H_{el} = -\frac{1}{2} \sum_i \nabla_i^2 + \frac{1}{2} \sum_{j \neq i} \frac{1}{|\mathbf{r}_i - \mathbf{r}_j|} - \sum_i \sum_I \frac{Z_I}{|\mathbf{R}_I - \mathbf{r}_i|} = T + V_{int} + V_{ext} \quad (2.6)$$

with atomic units, where  $\hbar = e = m_e = 1$ .  $V_{int}$  term is the reason why we cannot separate the wave function which depends on the quantum mechanical exchange-correlation effects.  $V_{ext}$  term represents the classical Coulomb interaction.

## 2.2 Pre-Density Functional Theory

### 2.2.1 Hartree and Hartree-Fock approximation

The main problem is solving the many-body Schrödinger equation in the external Coulomb field created by a number of atomic nuclei. Hartree used a product of single particle wave-

functions to represent the many body wavefunction in 1928 as a first approximation[38]. Approximate wave function is obtained from the variational principle,

$$\Phi(\mathbf{x}_1, \mathbf{x}_2, \dots, \mathbf{x}_N) = \phi_1(\mathbf{x}_1)\phi_2(\mathbf{x}_2), \dots, \phi_N(\mathbf{x}_N) \quad (2.7)$$

Hartree proposed one-particle Schrödinger equations as:

$$\left( -\frac{\hbar^2}{2m} \nabla^2 - V_{ext}(\mathbf{R}, \mathbf{r}) + \int \frac{\sum_{j \neq i}^N |\phi_j(\mathbf{r}')|^2}{|\mathbf{r} - \mathbf{r}'|} d\mathbf{r}' \right) \phi_i(\mathbf{r}) = \varepsilon_i \phi_i(\mathbf{r}) \quad (2.8)$$

On the left hand side the third term is called the Hartree potential and it is the classical electrostatic potential due to the other electrons. The effective potential,  $V_{eff}$ , is the sum of the second and third term on the left hand side, in which the electron-electron interaction had been counted twice. Therefore, to express the correct form of the energy we write

$$E_H = \sum_{i=1}^N \varepsilon_i - \frac{1}{2} \int \int \frac{\rho(\mathbf{r}_i)\rho(\mathbf{r}_j)}{|\mathbf{r}_i - \mathbf{r}_j|} d\mathbf{r}_i d\mathbf{r}_j \quad (2.9)$$

In order to solve the coupled Equations 2.8, first energy is minimized by using a trial wave function, then put them back to  $V_{eff}$  and solve again the Schrödinger equation and do it until the self-consistency is accomplished. This is the Hartree approximation in a self-consistent way. Due to electrons being fermion and Pauli exclusion principle the total electron wave function must be antisymmetric. Slater determinant is used to make antisymmetric many electron wave function.

$$\Phi_{HF}(x_1, x_2, \dots, x_N) = \frac{1}{\sqrt{N!}} \begin{vmatrix} \phi_1(1) & \phi_2(1) & \cdots & \phi_N(1) \\ \phi_1(2) & \phi_2(2) & \cdots & \phi_N(2) \\ \vdots & \vdots & \ddots & \vdots \\ \phi_1(N) & \phi_2(N) & \cdots & \phi_N(N) \end{vmatrix} \quad (2.10)$$

$$\Phi_{HF} = \frac{1}{\sqrt{N!}} \sum_{i=1}^N (-1)^{P(i)} \phi_{i_1}(\mathbf{x}_1)\phi_{i_2}(\mathbf{x}_2) \dots \phi_{i_N}(\mathbf{x}_N) \quad (2.11)$$

Hence, Hartree-Fock (HF) approximation can explain the exchange of particles.[39, 40].

### 2.2.2 Thomas-Fermi Theory

As an early quantum statistical model Thomas and Fermi proposed that electron density is the fundamental variable instead of the many-body wave function. They have presented a differential equation for the electron density, which did not depend on the one electron orbitals[41, 42]. Total energy expression as a functional of the electronic density, in Thomas-Fermi theory is given by:

$$E_{TF}[\rho] = C_k \int \rho(\mathbf{r})^{5/3} d\mathbf{r} + \int \rho(\mathbf{r}) v_{ext}(\mathbf{r}) d\mathbf{r} + \frac{1}{2} \int \int \frac{\rho(\mathbf{r})\rho(\mathbf{r}')}{|\mathbf{r} - \mathbf{r}'|} d\mathbf{r} d\mathbf{r}' \quad (2.12)$$

without exchange-correlation effect.

## 2.3 Modern Density Functional Theory

The beginning of modern density functional theory was constructed by two articles: Hohenberg-Kohn article [43] and Kohn-Sham article [44], in 1964 and in 1965, respectively. DFT suggests that, knowing the ground state density  $\rho(\mathbf{r})$  we can uniquely determine the system.

The electron density is a function which will give the probability of finding an electron at a particular place  $\mathbf{r}$  in space:

$$\rho(\mathbf{r}) = N \int |\psi(\mathbf{r}_1, \mathbf{r}_2, \dots, \mathbf{r}_N)|^2 d\mathbf{r}_2 d\mathbf{r}_3 \dots d\mathbf{r}_N \quad (2.13)$$

As any other observable, the electronic density is also obtained by using wave function. DFT makes the reverse case possible.

### 2.3.1 Hohenberg-Kohn Theory

The theorem is divided into two parts [43]:

**HK 1:** There cannot be  $v_{ext}(\mathbf{r}) \neq v'_{ext}(\mathbf{r})$  that corresponds to the same ground state electronic density, that is, the external potential is unequivocally obtained by the ground state density.

Therefore, for this  $v_{ext}(\mathbf{r})$ , the ground state wave function is a unique functional of the ground state electron density. Hence, we get the full Hamiltonian.

**HK 2:** The ground state energy for the system equals to the energy corresponding to the unique ground state density, which attains its minimum value

$$E_0[\rho(\mathbf{r})] = \int v_{ext}(\mathbf{r})\rho(\mathbf{r})d\mathbf{r} + F[\rho(\mathbf{r})] \quad (2.14)$$

where  $F[\rho(\mathbf{r})]$  is a universal functional independent from the  $V_{ext}(\mathbf{r})$  of the system, containing the kinetic energy and electron-electron interaction terms.

### 2.3.2 The Kohn-Sham equations

Kohn and Sham proposed an approach that the electron density is written in terms of Kohn-Sham orbitals[44], which are fictitious single particle orbitals and which are constructed to make the usage of Hohenberg-Kohn theorems possible in real system calculations.

$$\rho(\mathbf{r}) = \sum_i |\Phi_i(\mathbf{r})|^2 \quad (2.15)$$

The non-interacting system's Hamiltonian lowest order eigenfunctions are  $\Phi_i(\mathbf{r})$ . Here, the expression for the kinetic energy functional of electron density is problematic. In Kohn-Sham formalism, the kinetic energy of the interacting electrons is replaced by the kinetic energy of the equivalent non-interacting electrons which are experiencing an effective potential,  $V_{eff}$ [44]. Hence,  $V_{eff}$  mimics the interactions with the other electrons in addition to the ionic potentials.

$$V_{eff} = \int v_{ext}(\mathbf{r})\rho(\mathbf{r})d\mathbf{r} + \int \frac{\rho(\mathbf{r})\rho(\mathbf{r}')}{|\mathbf{r} - \mathbf{r}'|}d\mathbf{r}d\mathbf{r}' + V_{xc} \quad (2.16)$$

Kohn-Sham equations are single particle Schrödinger like equations:

$$H_{eff} = [T' + V_{eff}]\Phi_i(\mathbf{r}) = \epsilon_i\Phi_i(\mathbf{r}) \quad (2.17)$$



Here, the kinetic energy operator does not represent the kinetic energy for the interacting system and a correction is considered in the term  $V_{xc}$ .

$V_{eff}$  is dependent on the density. A self-consistent cycle is needed to solve Kohn-Sham equations, as in the Hartree approximation, in which we start with a trial density and make iterative calculations.

Universal functional  $F[\rho]$  is:

$$F[\rho] = T[\rho] + \int \int \frac{\rho(\mathbf{r})\rho(\mathbf{r}')}{|\mathbf{r} - \mathbf{r}'|} d\mathbf{r}d\mathbf{r}' + E_{XC}[\rho] \quad (2.18)$$

With this  $F[\rho]$  functional and Eq. 2.14 total energy functional is obtained as:

$$E_{KS}[\rho] = T[\rho] + \int \rho(\mathbf{r})v_{ext}(\mathbf{r})d\mathbf{r} + \frac{1}{2} \int \int \frac{\rho(\mathbf{r})\rho(\mathbf{r}')}{|\mathbf{r} - \mathbf{r}'|} d\mathbf{r}d\mathbf{r}' + E_{XC}[\rho] \quad (2.19)$$

which is known as the Kohn-Sham functional.

## 2.4 Functionals for Exchange and Correlation

Because of the Pauli exclusion principle the exchange-correlation effects are seen. In addition to the Coulomb forces, there are other attractive or repulsive forces resulting from the overlap of the antisymmetric wave functions.  $E_{xc}$  has a complicated nature. Therefore, to write the  $E_{xc}[\rho]$  functional there are approximations to be made. The most common approximations for the  $E_{xc}[\rho]$  functional are the localized density approximation (LDA) and generalized gradient approximation (GGA).

### 2.4.1 The Localized Density Approximation (LDA)

In LDA, the density is assumed to be locally homogeneous.  $E_{xc}^{LDA}[\rho]$  functional is obtained by integrating this local exchange-correlation energy functional of locally homogeneous density,  $\epsilon_{xc}^{hom}[\rho]$ .

$$E_{xc}^{LDA}[\rho] = \int \rho(\mathbf{r}) \epsilon_{xc}^{hom}[\rho(\mathbf{r})] d\mathbf{r} \quad (2.20)$$

Most commonly used LDA functionals are Perdew-Zunger (PZ) [45, 46], Perdew-Wang (PW) [47].

## 2.4.2 Generalized Gradient Approximation (GGA)

In order to improve the LDA, GGA approach includes in the integration also the gradient of the density:

$$E_{xc}^{GGA}[\rho] = \int \rho(\mathbf{r}) \epsilon_{xc}[\rho(\mathbf{r}), \nabla\rho(\mathbf{r})] d\mathbf{r} \quad (2.21)$$

Mostly used GGA functionals are Becke-Lee-Yang-Parr (BLYP) [48, 49] and Perdew-Burke-Enzerhof (PBE)[50].

## 2.5 Plane-wave Basis Set for Kohn-Sham Orbitals

Kohn-Sham orbitals  $\Phi_i(\mathbf{r})$  ought to be expanded using a finite basis set in order to solve the Kohn-Sham equations. This basis set is chosen as plane waves. Hence, the Kohn-Sham Hamiltonian takes a simpler form, that is, all the potentials are described by their Fourier transforms and the kinetic energy matrix is diagonal. We get the solution by diagonalizing the Kohn-Sham Hamiltonian matrix. The cutoff energy value determines the size of this matrix.

### 2.5.1 Bloch's Theorem

Because of the crystal structure plane-wave expansion of the  $\Phi_i(\mathbf{r})$  orbitals are possible. Due to regular arrangement of the ions in the crystal, the potential corresponding to this system is periodic. Bloch's theorem states that the wavefunctions in this potential will also be periodic with the same periodicity[51]. Hence, Schrödinger equations' eigenfunctions  $\Phi(\mathbf{r})$  can be written as a product of a cell periodic function,  $u(\mathbf{r}, \mathbf{k})$ , and a plane wave:

$$\Phi(\mathbf{r}) = u(\mathbf{r}, \mathbf{k})e^{i(\mathbf{k}\cdot\mathbf{r})} \quad (2.22)$$

The cell periodic function  $u(\mathbf{r}, \mathbf{k})$  can be written using the reciprocal lattice vectors of the crystal:

$$u(\mathbf{r}, \mathbf{k}) = \sum_{\mathbf{G}} a_{\mathbf{k}, \mathbf{G}} e^{i\mathbf{G}\cdot\mathbf{r}} \quad (2.23)$$

Therefore the wavefunction of the system is written as a sum of plane waves:

$$\Phi(\mathbf{r}) = \Phi_i(\mathbf{r}, \mathbf{k}) = \sum_{\mathbf{G}} a_{i, \mathbf{k}+\mathbf{G}} e^{i(\mathbf{k}+\mathbf{G})\cdot\mathbf{r}} \quad (2.24)$$

### 2.5.2 k-point Sampling

The electronic states considered here are possible on a set of  $\mathbf{k}$ -points, which are obtained by the boundary conditions. Depending on the volume of the cell the density of the allowed  $\mathbf{k}$ -points are determined. The discretization of the  $\mathbf{k}$ -point set is another approximation. There are several methods for obtaining the discretization[52, 53, 54, 55]. We will use Monkhorst-Pack scheme[54].

### 2.5.3 Plane-wave Representation of Kohn-Sham Equations

The system's wavefunction is expanded in terms of plane waves:

$$\Phi_i(\mathbf{r}, \mathbf{k}) = \sum_{\mathbf{G}_m} a_i(\mathbf{k}, \mathbf{G}_m) e^{i(\mathbf{k}+\mathbf{G}_m)\cdot\mathbf{r}} = \sum_{\mathbf{G}_m} a_i(\mathbf{k}, \mathbf{G}_m) |\mathbf{k} + \mathbf{G}_m \rangle \quad (2.25)$$

From the orthonormality condition for the plane waves we get:

$$\langle \mathbf{k} + \mathbf{G}_{m'} | \mathbf{k} + \mathbf{G}_m \rangle = \delta_{mm'} \quad (2.26)$$

Then the Kohn-Sham Hamiltonian from the Eq. 2.17 takes the form:

$$\sum_{\mathbf{G}_m} a_i(\mathbf{k}, \mathbf{G}_m) \langle \mathbf{k} + \mathbf{G}_{m'} | H_{eff} | \mathbf{k} + \mathbf{G}_m \rangle = \epsilon_i \sum_{\mathbf{G}_m} a_i(\mathbf{k}, \mathbf{G}_m) \delta_{mm'} = \epsilon_i \sum_{\mathbf{G}_m} a_i(\mathbf{k}, \mathbf{G}_{m'}) \quad (2.27)$$

and in a compact form it will be:

$$\sum_{\mathbf{G}_m} a_{i,m} H_{mm'} = \epsilon_i \sum_{\mathbf{G}_m} a_{i,m'} \quad (2.28)$$

If we consider the operators constituting the Kohn-Sham Hamiltonian separately:

First the kinetic energy operator:

$$\langle \mathbf{k} + \mathbf{G}_{m'} | T | \mathbf{k} + \mathbf{G}_m \rangle = - \langle \mathbf{k} + \mathbf{G}_{m'} | \frac{1}{2} \nabla^2 | \mathbf{k} + \mathbf{G}_m \rangle = \frac{1}{2} |\mathbf{k} + \mathbf{G}_m|^2 \delta_{mm'} \quad (2.29)$$

After that the effective potential matrix:

$$\langle \mathbf{k} + \mathbf{G}_{m'} | V_{eff}(\mathbf{r}) | \mathbf{k} + \mathbf{G}_m \rangle = \sum_{\mathbf{G}_m} V_{eff}(\mathbf{G}_m) \delta_{\mathbf{G}_m - \mathbf{G}_{m'}, \mathbf{G}_m} = V_{eff}(\mathbf{G}_m - \mathbf{G}_{m'}) \quad (2.30)$$

Then, the Kohn-Sham Hamiltonian becomes:

$$H_{mm'} = \frac{1}{2} |\mathbf{k} + \mathbf{G}_m|^2 \delta_{mm'} + V_{eff}(\mathbf{G}_m - \mathbf{G}_{m'}) \quad (2.31)$$

Here, the sum could be truncated at a cutoff energy value,  $E_{cut}$ , [56] since plane waves are negligible for large numbers of  $\mathbf{G}$ . The smallest possible cutoff energy value giving the accurate results can be determined by applying convergence tests for a range of cutoff energy values. Therefore, the size of the Kohn-Sham Hamiltonian matrix is determined by the value of  $E_{cut}$ , which will be extremely large for real systems consisting of core and valence electrons. And this is overcome by pseudopotential approximation.

## 2.6 Pseudopotentials

In electronic structure calculations, the ‘‘pseudopotential’’ concept is connected to replacing the effects of the nucleus Coulomb potential on the tightly bound core electrons with an ef-

fective potential acting on the valence electrons. Core electron states are assumed unchanged. Therefore, the pseudopotentials are used for computing the properties of the valence electrons resulting from these core electron states.

The potential has a oscillating behavior in the vicinity of the ions. Hence, the wave function has the same oscillating behavior. To represent this oscillations the expansion of the wave function requires a large number of plane waves. Nevertheless, at a certain radius,  $r_c$ , the wavefunction tends to become smooth in which the behavior of the wave function is determined by the valence electrons. This smooth wave function is represented by only a few plane waves. Replacing the oscillatory core part with smoother pseudopotentials makes sense, since almost all physical or chemical properties of any material are dependent on the behavior of the valence electrons. Therefore, only the valence electrons' density is taking into account in DFT calculations.

Norm-conserving property is required for the pseudopotentials, which states that integrated charge inside  $r_c$  for the real and pseudo wave functions must be the same. But the norm-conserving property can be eased to obtain smoother pseudopotentials, which will shorten the computational time. Ultrasoft pseudopotentials[21] can be an example of pseudopotentials not obeying the norm-conserving property.

## CHAPTER 3

### GaAs/AlAs BULK HETEROSTRUCTURE SYSTEM

In this chapter, we make an extensive analysis of GaAs/AlAs bulk heterostructure (HET) system including the electronic band structures at the interfaces within the formalism of DFT as thoroughly reported in Chapter 2. The most important parameters characterizing heterostructure systems are the valence- and conduction-band discontinuities. Several studies have been made about the band-offsets in lattice-matched heterostructures depending on the first-principles calculations. In these studies they have searched for the lineup of the average electrostatic potential through the interface, and the band offset is obtained by addition of this potential shift with the bulk band-edge difference.

#### 3.1 Method

Density functional theory ensures a fundamental theoretical framework to address the band lineup problem. Our calculations are carried out using PWSCF package program [22]. We use the LDA for the exchange-correlation potential as implemented by Perdew and Zunger [45] and Ceperley and Alder [46]. In the LDA, exchange-correlation functional is a function of the local charge density [44]. In such a pseudopotential approach only the valence electrons are considered and the pseudopotential, which is obtained from LDA-SCF calculations [57]. A plane-wave basis set is used to expand the single-particle electronic orbitals for periodic solids [56]. The reciprocal space formulation is dependent on the plane wave basis set [58, 59, 60]. Integrals over the Brillouin zone (BZ) are carried out by discrete summation over the special  $\mathbf{k}$ -points [52, 53, 54, 55].

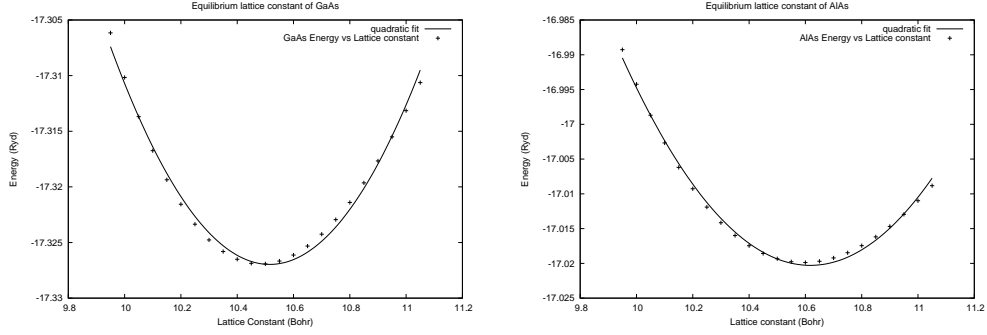


Figure 3.1: Equilibrium lattice constant of GaAs and AlAs.

### 3.2 Bulk properties of GaAs and AlAs

As a preliminary step towards the study of the GaAs/AlAs heterostructure we have analyzed the properties both of bulk GaAs and of bulk AlAs within the formalism of DFT. GaAs and AlAs are binary compound semiconductors from the III-V group in the zinc blende structure. For Ga, Al and As we have used the norm-conserving pseudopotential of Perdew and Zunger [45] to describe the interaction between valence electrons and ionic cores.

Depending on the convergence tests for the total energy of bulk GaAs with respect to the energy cutoff and to  $\mathbf{k}$ -point sampling at the calculated lattice constant the plane wave basis set used has a kinetic energy cutoff 20 Ry and the BZ integration is performed using a uniform Monkhorst-Pack [54] [10X10X10] grid. The equilibrium lattice constants have been calculated as 10.52 a.u.(=5.57Å) (experimentally 10.683 a.u.) for GaAs and 10.62 a.u.(=5.62Å) (experimentally 10.698 a.u.) shown in Fig. 3.1 with LDA (The equilibrium lattice constant have been calculated as 10.80 a.u. for GaAs with GGA). We have checked that the energy cutoff and the  $\mathbf{k}$ -point grid values are sufficient for getting accurate results (converged within almost 1%). As shown in Table 3.1 the difference with experimental values for the lattice parameter is in good agreement. The valence band maximum for GaAs is 5.1200eV and for AlAs is 5.1276eV, VBM values and band gap values for GaAs and AlAs are shown in Table 3.2.

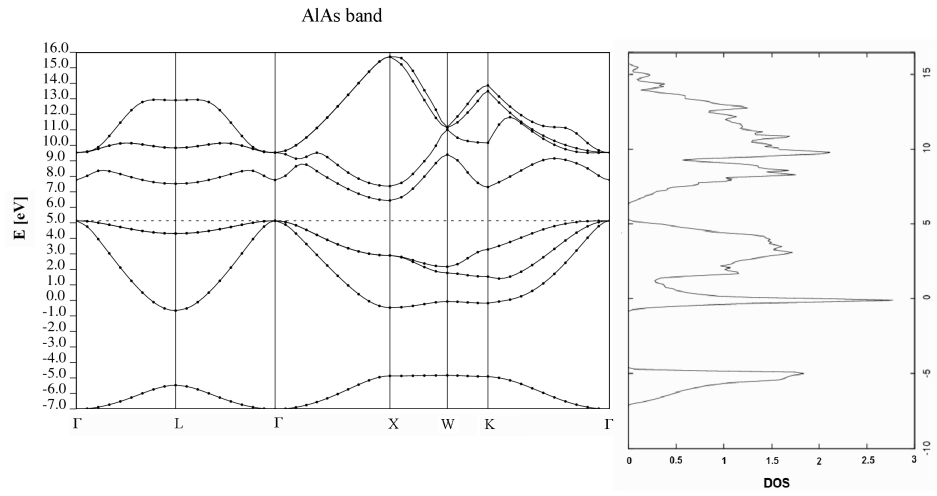


Figure 3.2: AlAs band structure and DOS

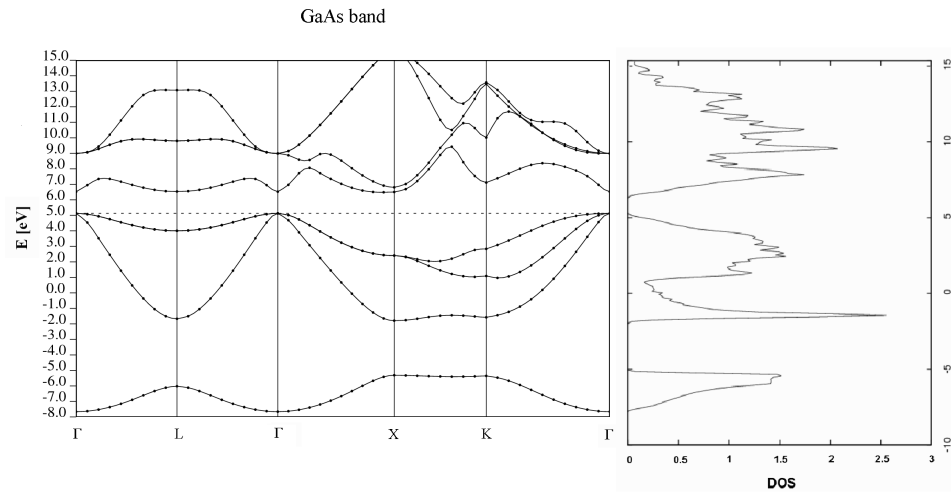


Figure 3.3: GaAs band structure and DOS

Table 3.1: Lattice parameters for GaAs and AlAs

Type	$a_o$ (a.u.)	$a_o^{exp}$ (a.u.)	difference
GaAs	10.52	10.683	1.6%
AlAs	10.62	10.698	0.8%



Table 3.2: Valence band maximum and band gap for GaAs and AlAs

Type	VBM(eV)	$E_g$ (eV)
GaAs	5.4127	1.3244
AlAs	5.4021	1.2541

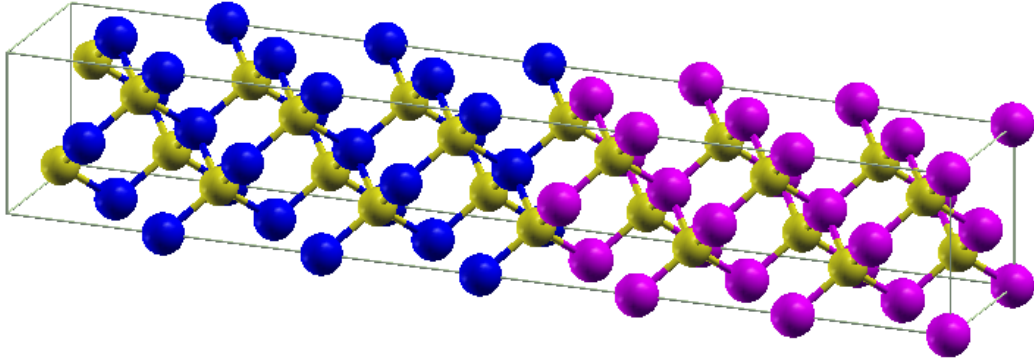


Figure 3.4:  $(GaAs)_3(AlAs)_3$  oriented along the direction (100) interface simulated by a 6+6 superlattice where Ga, Al, As atoms are shown by purple, dark blue and yellow circles, respectively.

### 3.3 GaAs/AlAs(001) heterostructure

For the heterostructure system, the atomic positions were allowed to relax for atoms to take their minimum energy configuration. Bulk heterostructure (HET) unit cell with 6+6 (i.e.  $(GaAs)_3(AlAs)_3$ ) period is given in Fig. 3.4, which is oriented in (001) direction, and which is drawn by XCrySDEN (Crystalline Structures and Densities) program [61]. For all the calculations relating  $(GaAs)_3(AlAs)_3$  HET system we use a 50Ry energy cutoff. Brillouin zone sampling is performed using a [18x18x3] Monkhorst-Pack grid [54].

The difference between our computationally calculated lattice constants of GaAs and AlAs is  $0.05 \text{ \AA}$  while the difference obtained in the experiments is just  $0.008 \text{ \AA}$ , which means there is a slightly overestimated strain in our calculations.

### 3.4 Theoretical study of band-offsets at the interface

We have calculated the interface band offset of GaAs/AlAs system from first-principles. From a heterostructure calculation estimating the change in the average electrostatic potential through the interface and then aligning the bulk valence band maximum (VBM) of two semiconductor constituents according to this average electrostatic potential will give us the valence-band offset (VBO). Baldereschi *et al.* [30] have calculated the xy planar averaged potential by taking the average in the growth direction to get a curve for the potential which is varying slowly, from where potential shifts have been obtained. The experimental data for the VBO in GaAs/AlAs range from 0.40 eV to 0.55 eV. [65] Baldereschi *et al.* [30] have calculated the offset for (100), (110) and (111) interfaces in between 0.49-0.51 eV, which is within the experimental error bar.

We have used the average electrostatic potential technique of [30] to get the valence-band offset in  $(GaAs)_3(AlAs)_3(001)$  superlattices. To sum up, in order to calculate the band offset we need to consider two contributions: the potential shift at the interface and the difference between the valence band maximum of bulk GaAs and AlAs calculated from independent calculations, as described in Section 3.2.

Our calculations are performed on a superlattice geometry. The interface characteristics are studied using a few atomic planes of each GaAs and AlAs materials. Supercells contain two interfaces, so we get the isolated interface configuration by making the adjacent interfaces separated from each other. The 6+6 superlattice is shown in Fig. 3.4, here GaAs/AlAs interface has been simulated by a 6+6 superlattice, through periodically repeating and alternating slabs of GaAs and AlAs and from the self-consistent calculations we get the charge density and electrostatic potential. Since planes parallel to the interface are periodic we have obtained planar averages of charge density and the corresponding electrostatic potential as a function of the direction perpendicular to the interface, which is z coordinate, the growth direction:

$$\bar{f}(z) = \frac{1}{S} \int_S f(x, y, z) dx dy \quad (3.1)$$

where S is the area of the (x, y) plane. So we can have the one dimensional charge density  $\bar{\rho}(z)$  and electrostatic potential  $\bar{V}(z)$  from the three dimensional electronic charge density. If we

look at the plot of these planar averages of  $\bar{\rho}(z)$  and  $\bar{V}(z)$  we get periodic functions in GaAs and AlAs materials, smoothly joining across the interface. For the GaAs/AlAs HET system, which is a lattice-matched one, on each side of the interface the period of these periodic functions of  $\bar{\rho}(z)$  and  $\bar{V}(z)$  are the same, which is the half of the bulk lattice parameter. There is a slight difference between these periodic functions due to the effect of the interface which could be enhanced by excluding the bulk-like variations using the macroscopic average technique, which is the one dimensional average of  $\bar{f}$  over a period centered at  $z$ :

$$\bar{\bar{f}}(z) = \frac{1}{\alpha} \int_{z-\alpha/2}^{z+\alpha/2} \bar{f}(z') dz' \quad (3.2)$$

where  $\alpha$  is the interplanar distance along the  $z$  direction.

There is no oscillation on the two part of the interface for the macroscopically averaged quantities, and we get a constant limit in each part of the heterostructure which shows that the potential experienced by a carrier in layers of lattice-matched heterostructures is the same as in the bulk material except at the interface there is a shift because of the two dimensional dipole layer. Therefore, in the interface region deviations are seen from this macroscopic limit. The potential shift can be obtained from this slowly varying curve, as 0.54 eV from this slowly varying curve for the potential, as seen in Fig. 3.5. The valence-band maximum is at  $E_v[GaAs]=5.4127$  eV in the bulk GaAs and  $E_v[AlAs]=5.4021$  eV in the bulk AlAs, so the difference is 0.0106 eV. Therefore the net offset is 0.55 eV, which is close to the experimental value [64] of 0.53 eV.

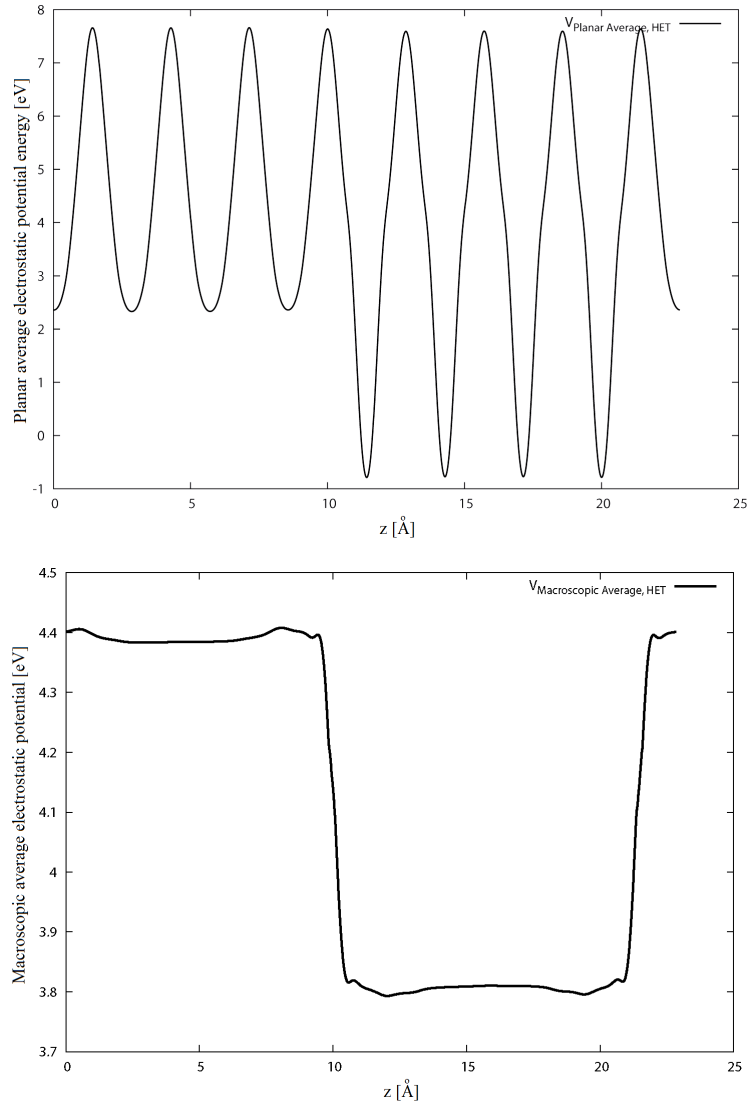


Figure 3.5: For  $(GaAs)_3(AlAs)_3$  superlattices the planar average and macroscopic average of electrostatic potential along the growth direction is shown, respectively.  $\Delta V$  corresponds to the difference between the plateaus, which is 0.54 eV in here.

## CHAPTER 4

### GaAs/AlAs NANOWIRE HETEROSTRUCTURE SYSTEM

In this chapter, we make an extensive analysis of GaAs/AlAs NWHETs for further studies in addition to experimental and theoretical studies of the bulk heterostructure system. To this end we make a first-principles search on structural and electronic properties GaAs/AlAs NWHETs grown along [001] and [111] directions. The bare GaAs/AlAs nanowire having  $N$  atoms is represented by GaAs/AlAsNWHET( $N$ ). The hydrogen passivated GaAs/AlAs nanowire is represented by H-GaAs/AlAsNWHET( $N$ ).

#### 4.1 Method

Our calculations are carried out using the PWSCF code suite [22]. We use the LDA for the exchange-correlation potential as implemented by Perdew and Zunger [45] and Ceperley and Alder [46]. In the LDA, exchange-correlation functional is a function of the local charge density [44]. In such a pseudopotential approach only the valence electrons are considered and the pseudopotential, which is obtained from LDA-SCF calculations [57]. A plane-wave basis set is used to expand the single-particle electronic orbitals for periodic solids [56]. The reciprocal space formulation is dependent on the plane wave basis set [58, 59, 60]. Integrals over the Brillouin zone (BZ) are carried out by discrete summation over the special  $\mathbf{k}$ -points [52, 53, 54, 55].

All nanowires studied here are constructed by selecting an axis along a crystallographic direction in bulk zinc blende and taking the atoms which are in a chosen distance from the nanowire axis. Besides GaAs and AlAs nanowires we also consider a nanowire with a periodic repetition of a couple of GaAs and AlAs planes, constituting a GaAs/AlAs nanowire

heterostructure. The geometry is shown in Fig. 1.1, constructed by the repetition of three layers of GaAs and three layers of AlAs. The H-terminated nanowires are obtained by saturating the surface dangling with hydrogen. For all nanowire structures the lattice parameter and atomic positions were relaxed.

## 4.2 GaAs and AlAs nanowires

As a preliminary step towards the study of GaAs/AlAs nanowire heterostructure we have analyzed the properties both of GaAs nanowire and of AlAs nanowire within the formalism of DFT. GaAs and AlAs nanowires are formed by taking a slab of GaAs and taking the atoms which is in a certain radius that we choose and centered in the mean of the atoms in that slab. We use the LDA for the exchange-correlation potential as implemented by Ceperley and Alder [46] and Perdew and Zunger [45]. To compensate the partial occupancies we use the Gaussian smearing method with a smearing width of 0.01 Ry for atomic relaxation, and 0.001 Ry for band structure calculations.

GaAs nanowire superlattices are separated from their periodic repetitions by a region of vacuum, where the cell length along the x and y directions perpendicular to the wire is given by 27.52 Å in order to isolate the wires from their hypothetical neighbors and to prevent the overlap of the wave function with that in an adjacent wire. The radius of the nanowires are 5 Å and they lie along the z-axis, 2 lattice constant in length in this direction. For the nanowire systems, the atomic positions were allowed to relax for atoms to take their minimum energy configuration. For all the calculations relating the GaAs and AlAs nanowire systems we use a 50Ry energy cutoff. Brillouin zone sampling is performed using a [1X1X20] Monkhorst-Pack grid [54].

The bare GaAs nanowire having N atoms is represented by GaAsNW(N). The hydrogen passivated GaAs nanowire is represented by H-GaAsNW(N). In Fig. 4.1, Fig. 4.2, Fig. 4.3 and Fig. 4.4 the bare GaAs nanowire and the H-terminated GaAs nanowire along the [001] and [111] direction are shown, respectively. As seen in the figure, after relaxation GaAs nanowire surfaces undergo a reconstruction but inner parts remains in the bulk configuration. Similarly, in Fig. 4.5 and in Fig. 4.6 the bare and H-terminated AlAs nanowire oriented along the [111] direction are shown.

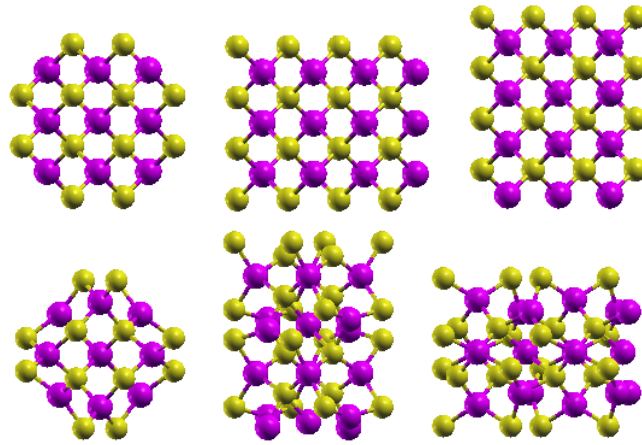


Figure 4.1: Relaxed bare GaAs nanowire oriented along the [001] direction: GaAsNW(42), where Ga and As atoms are shown by purple and yellow circles, respectively.

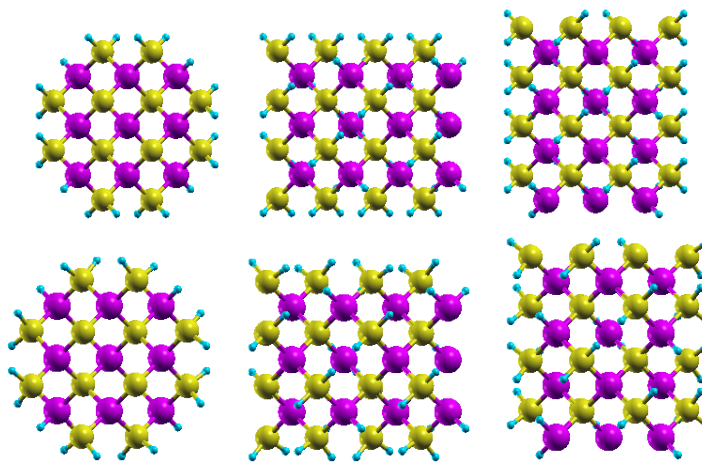


Figure 4.2: H-passivated GaAs nanowire oriented along the [001] direction: H-GaAsNW(82), where Ga, As, and H atoms are represented by purple, yellow and light blue circles, respectively.

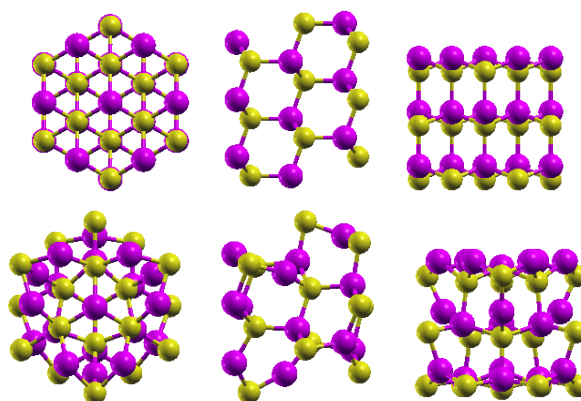


Figure 4.3: Relaxed bare GaAs nanowire oriented along the  $[111]$  direction: GaAsNW(38), where Ga and As atoms are represented by purple and yellow circles, respectively.

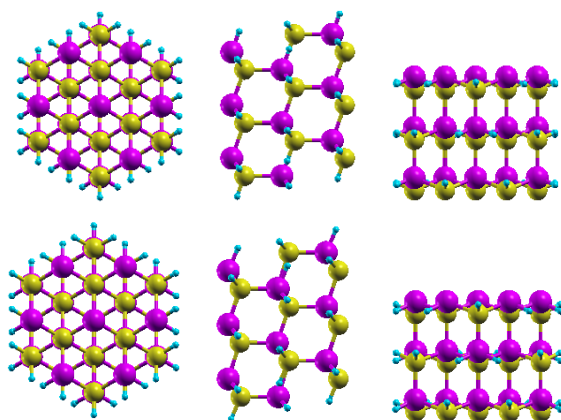


Figure 4.4: H-passivated GaAs nanowire oriented along the  $[111]$  direction: H-GaAsNW(68), where Ga, As, and H atoms are represented by purple, yellow and light blue circles, respectively.



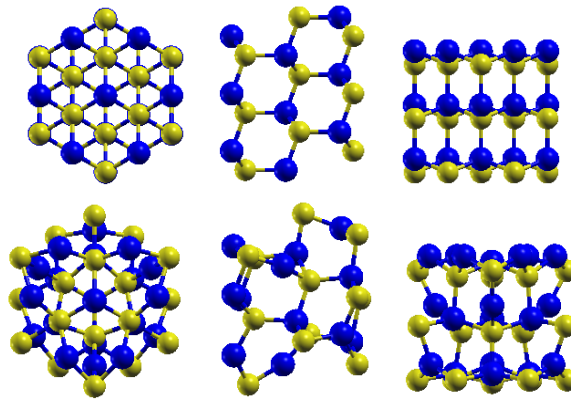


Figure 4.5: AlAs NW(38) along  $[111]$  direction and side views, where Al and As atoms are represented by dark blue and yellow circles, respectively. The surface reconstruction along this direction is in the second line.

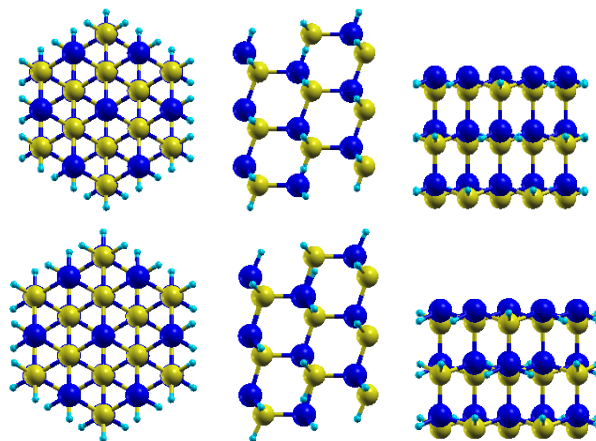


Figure 4.6: H-passivated AlAs nanowire oriented along the  $[111]$  direction: H-AlAsNW(68), where Al, As, and H atoms are represented by dark blue, yellow and light blue circles, respectively.

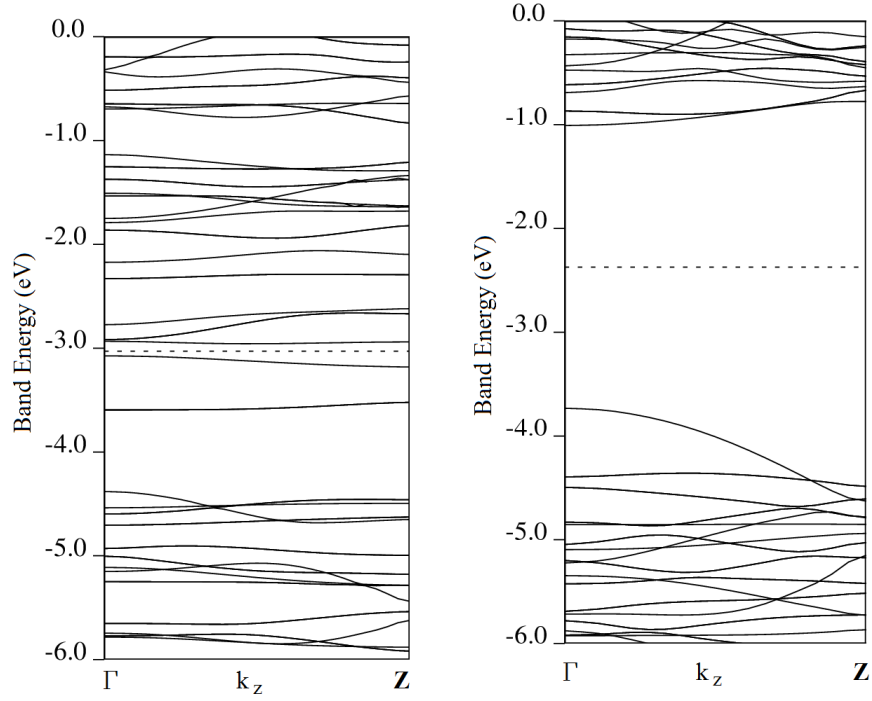


Figure 4.7: Band structures of GaAsNW(38) and H-GaAsNW(68) in [111] direction with surface dangling bonds not passivated and passivated with hydrogenlike pseudoatoms, respectively. The surface states are removed from the band gap when the surface dangling bonds have been passivated.

It is seen in Fig. 4.7, for GaAs nanowire oriented along the [111] direction after the surface dangling bonds have been passivated by hydrogenlike pseudoatoms the band gap is cleaned from surface states, which shows the localized surface states are the dangling bond states. Similarly, in Fig. 4.8 the band structures of bare and H-passivated AlAs nanowire oriented along the [111] direction are shown, representing that the localized surface dangling bond states are not in the band gap anymore.

To calculate the cohesive energy we have taken the difference between the total energy of the wire and the total energy of the same number of isolated atoms. The energy of an isolated Ga atom, an isolated Al atom, and an isolated As atom are calculated in a large enough unit cell. For the Ga atom, we have used  $16 \text{ \AA}^3$  cubic cell and we get an energy of  $-57.73 \text{ eV}$ . Also for the Al and As atom, we have used  $16 \text{ \AA}^3$  cubic cell and we get an energy of  $-52.90 \text{ eV}$  and  $-169.58 \text{ eV}$ , respectively. For the H atom, we have used  $21 \text{ \AA}^3$  cubic cell and we get an energy of  $-12.90 \text{ eV}$ . The cohesive energy per Ga-As pair of bare GaAsNW are calculated by

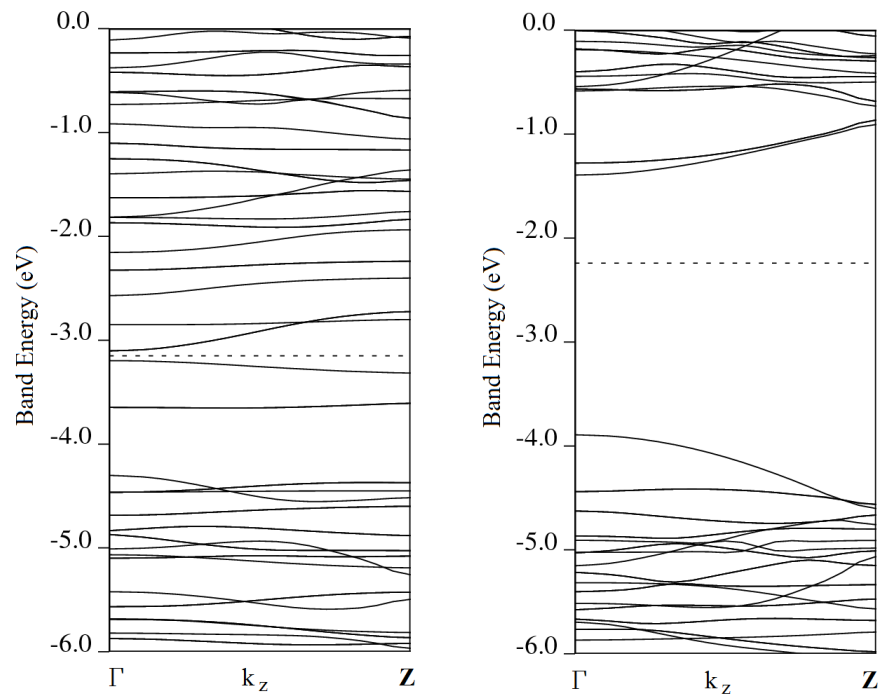


Figure 4.8: Band structures of AlAsNW(38) and H-AlAsNW(68) in [111] direction with surface dangling bonds not passivated and passivated with hydrogenlike pseudoatoms, respectively. The surface states are removed from the band gap when the surface dangling bonds have been passivated.

Table 4.1: The lattice constant  $a_0$  and the cohesive energy per Ga-As (Al-As) atom pair values for GaAs (AlAs) nanowires in the [111] direction, using Eq. 4.1 and Eq. 4.2

Type	$a_0$ (Å)	$E_c$ (eV)	$E'_c$ (eV)
GaAsNW(38)	5.62	7.33	-0.97
AlAsNW(38)	5.64	7.97	-1.07
GaAsNW(122)	5.53	7.83	-0.47
AlAsNW(122)	5.55	8.46	-0.57

Table 4.2: The binding energy of hydrogen for GaAs (AlAs) nanowires in the [111] direction with respect to the free H atom, using Eq. 4.3

Type	$E_b$ (eV)
H-GaAsNW(68)	4.18
H-AlAsNW(68)	4.39
H-GaAsNW(176)	4.27
H-AlAsNW(176)	4.48

$$E_c = (E_T[Ga] * N_{Ga} + E_T[As] * N_{As} - E_T[GaAsNW(N)])/N_{pair} \quad (4.1)$$

using the total energy of free Ga and As atoms and the total energy of GaAsNW(N) nanowire.  $E_c > 0$  implies that the structure is stable depending on the free Ga and As atoms. The cohesive energy with respect to the bulk crystal GaAs and AlAs is calculated by,

$$E'_c = E_T[bulkGaAs] - E_T[GaAsNW(N)]/N_{pair} \quad (4.2)$$

Calculated lattice constant  $a_0$  and cohesive energies are shown in Table 4.1.

The binding energy of hydrogen relative to the free H atom is calculated by,

$$E_b = (E_T[H] * N_H + E_T[GaAsNW(N)] - E_T[H - GaAsNW])/N_H \quad (4.3)$$

using the total energy of GaAsNW(N) and H-GaAsNW(N) nanowires and free H atom energy,  $E_T[H]$ . The values are shown in Table 4.2.

### 4.3 Modelling GaAs/AlAs Nanowire Heterostructure System with Supercell

GaAs and AlAs nanowires are formed by taking a slab of bulk GaAs in one crystallographic direction and taking the atoms which is in a certain radius that we choose and centered in the mean of the atoms in that slab. In order to form the nanowire heterostructures (NWHETs) the nanowire superlattices are made from repeating GaAs/AlAs layers along the longitudinal, that is, along the chosen crystallographic direction. All calculations are carried out using PWSCF package program [22]. We use the LDA for the exchange-correlation potential as implemented by Ceperley and Alder [46] and Perdew and Zunger [45]. To compensate the partial occupancies we use the Methfessel-Paxton smearing method [62] with a smearing width of 0.01 Ry for atomic relaxation, and 0.001 Ry for band-structure calculations. These NWHETs are separated from its periodic repetitions by a region of vacuum, where the cell length along the x and y directions perpendicular to the wire is given by 27.52 Å in order to isolate the wires from their hypothetical neighbors and to prevent the overlap of the wave function with that in an adjacent wire. The radius of the nanowires are 5 Å and they lie along the z-axis, 2 lattice constant in length in this direction. For nanowire heterostructure systems, the atomic positions were allowed to relax for atoms to take their minimum energy configuration. For all the calculations relating the GaAs/AlAs NWHET system we use a 50 Ry energy cutoff. Brillouin zone sampling is performed using a [1X1X30] Monkhorst-Pack grid [54]. In Fig. 4.9 GaAs/AlAs NWHET supercell in the x-y plane is shown.

### 4.4 Bare and H-passivated GaAs/AlAs Nanowire Heterostructures

In this section, firstly the bare and H-terminated GaAs/AlAs nanowire heterostructures oriented along [001] and [111] directions having different number of Ga, Al, As atoms are studied. Initially, GaAs/AlAs NWHETs are cut out from bulk GaAs/AlAs heterostructure. The initial atomic positions in bulk structure is allowed to relax to obtain the minimum total energy. Hydrogen passivation is performed by termination of surface dangling bonds. The properties of H passivated nanowire heterostructure system are different from the bare nanowire heterostructure system. We have examined in which way the hydrogen saturation of dangling bonds of surface atoms effects the electronic structure of the nanowire. Also the possible surface reconstruction is taken into account through relaxation.

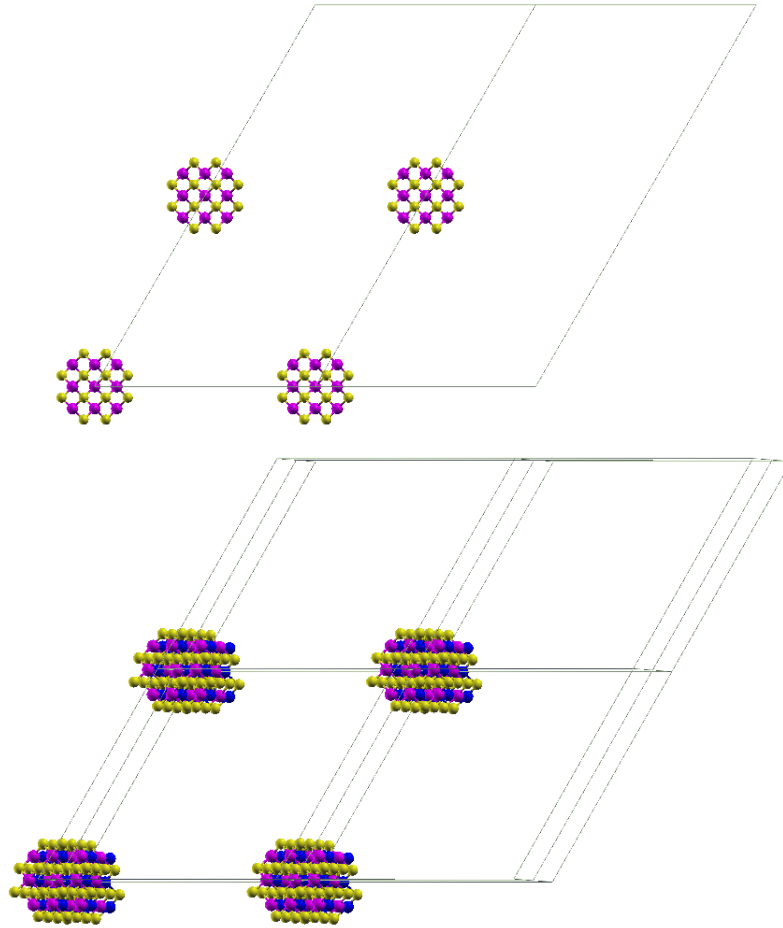


Figure 4.9: GaAs/AlAs NWHET supercell in the x-y plane and slightly off-axis where Ga, Al, As atoms are represented by purple, dark blue and yellow circles, respectively.

#### 4.4.1 Atomic Structure and Energetics

In Fig. 4.10 the cross section of NWHET(42), in direction [001] with diameter 5 Å is shown before and after relaxation. It is observed that after the relaxation the surface of the wire undergo a reconstruction, but the inner parts remain in bulk configuration. In the bulk part of GaAs and AlAs there are  $sp^3$  hybridized orbitals. Cations, which are at the surface of the nanowire, favors  $sp^2$ -like hybridization since they lost an electron. Because of that all Ga and Al atoms at the surface of the nanowire relaxes inward. After the electron transfer the dangling bond on the As atom is filled and As atom relaxes outward. In Fig. 4.11 the charge density contour plots of this reconstructed NWHET(42) along [001] direction is presented.

In Fig. 4.14 hydrogen passivated surface of H-NWHET(82) along [001] direction and in Fig. 4.15, hydrogen passivated surface of H-NWHET(136) along [111] direction are shown, that is, pseudohydrogen is used to saturate the surfaces of the nanowire. Here the pseudohydrogen represents a non-integer core charge  $Z$ . The dangling bond states on the surface of a semiconductor in nanoscale are electronically active states. Surface passivation with some passivation agent is needed without harming the neutrality of the system. Aim of the surface passivation is cleaning the band gap from the localized surface states [63].

In theoretical calculations hydrogen is used as passivation agent for group IV semiconductors. The bonds for II-VI and III-V are different from the bonds in group IV semiconductors. For III-V semiconductors the passivation by ordinary hydrogen is not enough as explained by Chelikowsky [63], where it is told that the best result is obtained by the use of pseudohydrogen atom ( $H^*$ ) where  $Z$  for  $H^*$  is different than 1, such as  $H^*$  ( $Z=1.25$ ) and  $H^*$  ( $Z=0.75$ ) for cations and anions, respectively. In Fig. 4.13 it is seen that the bonds with hydrogen atoms, with  $Z=0.5$ , on the cations are broken and in the second part of the figure it is seen that the bonds with hydrogen atoms, with  $Z=1$ , on the anion atoms are broken. . The relaxation results of saturation of nanowire surface with pseudohydrogen with  $Z=1.25$  for all surface Ga and Al atoms and with  $Z=0.75$  for all surface As atoms are shown in Fig. 4.14 and Fig. 4.15.

We now have the correct geometry for GaAs/AlAsNWHET and the total energy of the system. We can obtain the cohesive energy of the structure. The cohesive energy per Ga-As and Al-As pairs of bare GaAs/AlAs NWHETs are calculated by

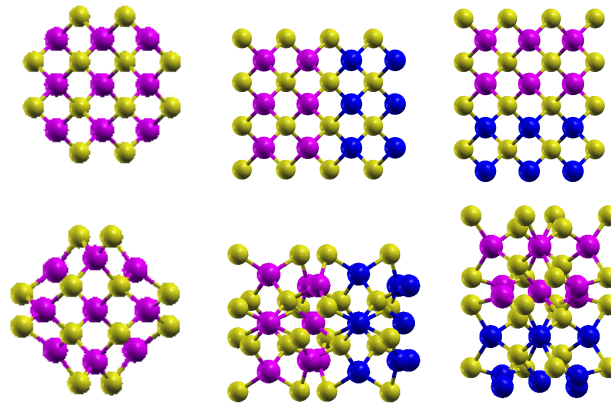


Figure 4.10: Surface reconstruction of GaAs/AlAs NWHET along [001] direction. Ga, Al, As atoms are represented by purple, dark blue and yellow circles, respectively.

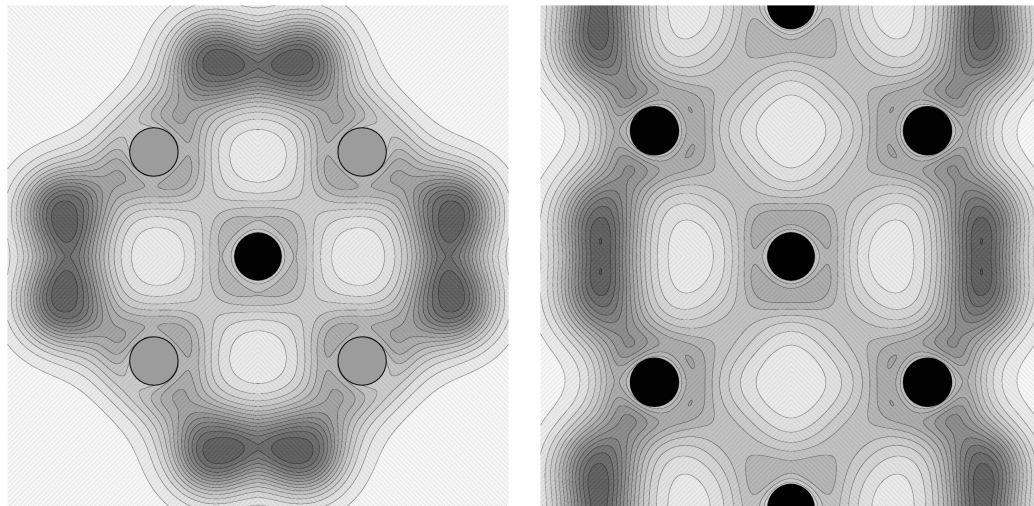


Figure 4.11: Charge density contour plots of reconstructed GaAs/AlAs NWHET along [001] direction, lateral plane is shown in left panel and vertical plane is in right plane.



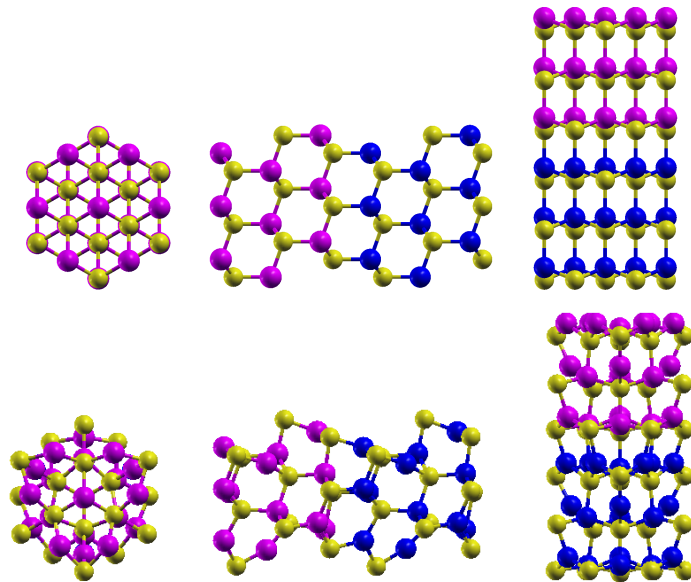


Figure 4.12: GaAs/AlAs NWHE(76) along  $[111]$  direction and side views. The surface reconstruction along this direction is in the second line.

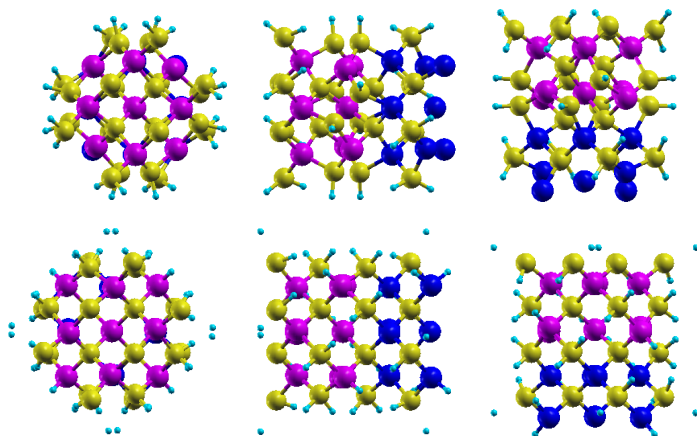


Figure 4.13: When  $Z=0.5$  the pseudohydrogen bond in the cations are broken, when  $Z=1$  the hydrogen bond in the cation atoms are broken.

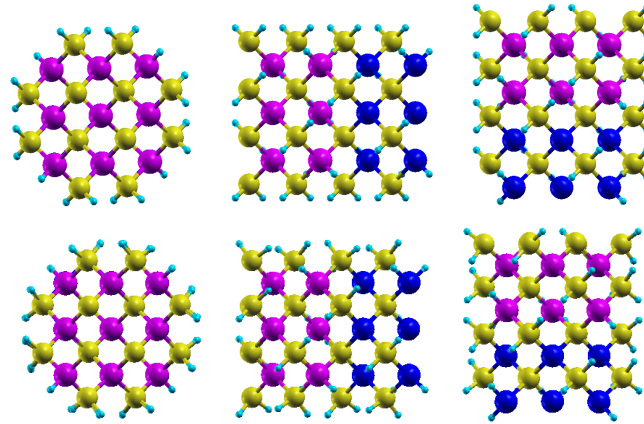


Figure 4.14: Relaxed GaAs/AlAs NWHET(82) oriented along the [001] crystallographic direction with the termination of dangling bonds with H-atom. Ga, Al, As, H atoms are represented by purple, dark blue, yellow and light blue circles, respectively. The relaxed structure in the second line is when  $H^*$  ( $Z=1.25$ ) and  $H^*$  ( $Z=0.75$ ) for cations and anions, respectively.

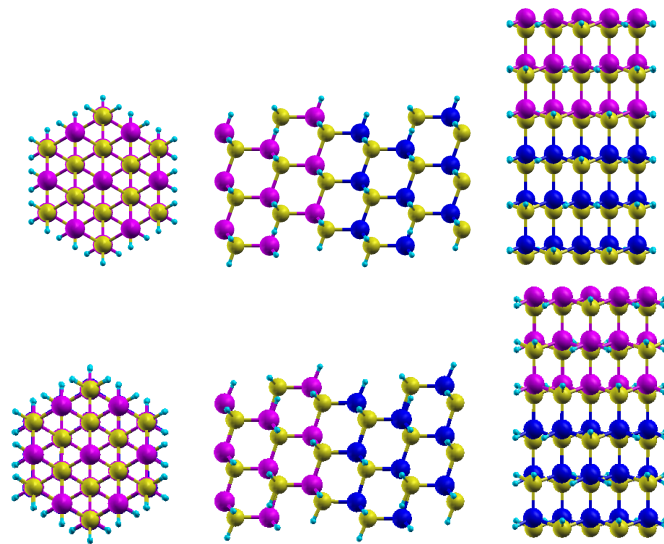


Figure 4.15: H-GaAs/AlAs NWHET(136) along [111] direction and side views of it with the termination of dangling bonds by H-atom and in the second line the relaxed coordinates are shown when  $H^*$  ( $Z=1.25$ ) and  $H^*$  ( $Z=0.75$ ) for cations and anions, respectively.

$$E_c = (E_T[Ga]*N_{Ga} + E_T[Al]*N_{Al} + E_T[As]*N_{As} - E_T[GaAs/AlAsNWHET(N)]) / N_{pair} \quad (4.4)$$

using the total energy of free Ga, Al and As atoms, number of Ga-As, Al-As pairs  $N_{pair}$  and the total energy of GaAs/AlAs NWHET(N), which gives an energy of 7.65 eV per pair in the [111] direction.  $E_c > 0$  makes sure that the structure is stable relative to free Ga, Al and As atoms.

The binding energy of hydrogen relative to the free H atom is calculated by,

$$E_b = (E_T[H]*N_H + E_T[GaAs/AlAsNWHET(N)] - E_T[H-GaAs/AlAsNWHET]) / N_H \quad (4.5)$$

using the energy of free H atom,  $E_T[H]$ , the total energy of GaAs/AlAs NWHET(N) and H - GaAs/AlAs NWHET (N) nanowires. To calculate the energy of an isolated H atom we have used 21 Å cubic cell and we get an energy of -12.90 eV. For the binding energy of H in the H - GaAs/AlAs NWHET (136) system oriented along the [111] crystallographic direction, we get 4.35 eV.

#### 4.4.2 Band Structure and Band Offset of GaAs/AlAs Nanowire Heterostructures

It is seen in Fig. 4.16 and Fig. 4.17 that after the surface dangling bonds of the NWHET system have been terminated by hydrogenlike pseudoatoms, the band gap is cleared from the surface states.

The determination of band offsets at interfaces of heterostructures is a requirement for semiconductor device design since, by controlling the band offsets, we can control the charge carrier flow and confinement. Band offsets have been calculated by using moderately refined methods at the interfaces of bulk heterostructures. At the semiconductor interface there is a charge accumulation because of aligning of Fermi levels. This charge accumulation creates an electric field and afterwards a potential is created at semiconductor interface. A heterostructure calculation estimating the shift in the average potential across the interface and then aligning the bulk valence-band maximum (VBM) of two semiconductor constituents according to this average electrostatic potential will give us the valence-band offset (VBO).

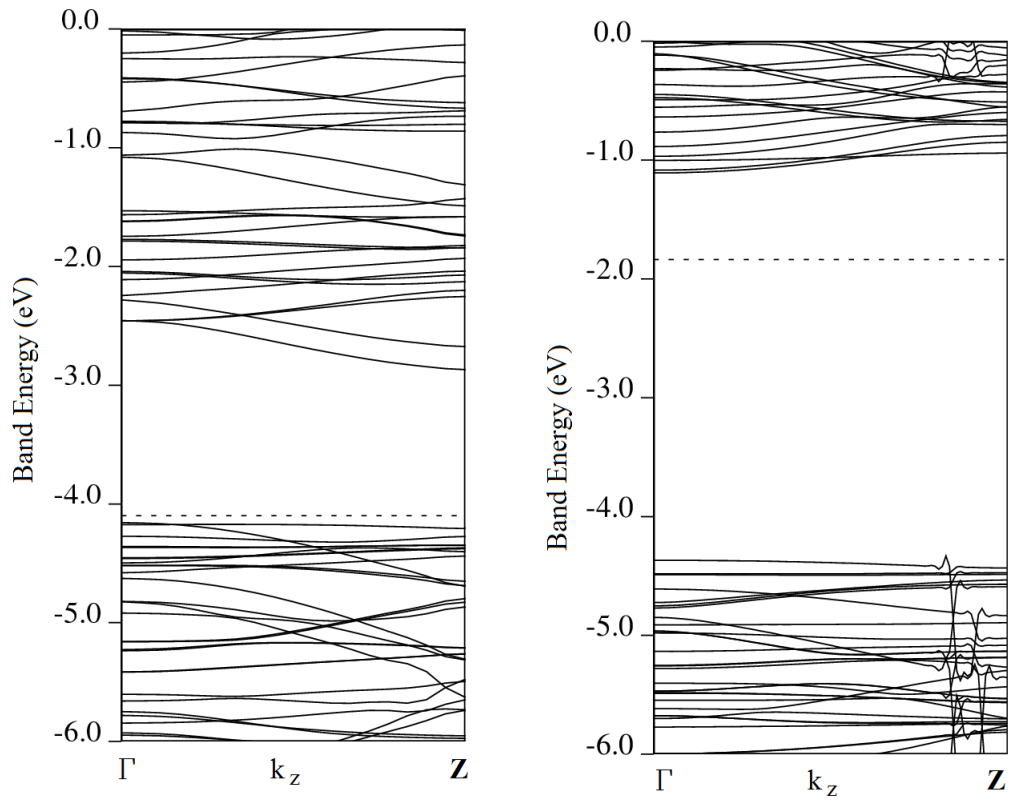


Figure 4.16: Band structures of GaAs/AlAs NWHE(42) and H-GaAs/AlAs NWHE(82) in [001] direction with surface dangling bonds not passivated and passivated with hydrogen-like pseudoatoms, respectively. The surface states are removed from the band gap when the surface dangling bonds have been passivated.

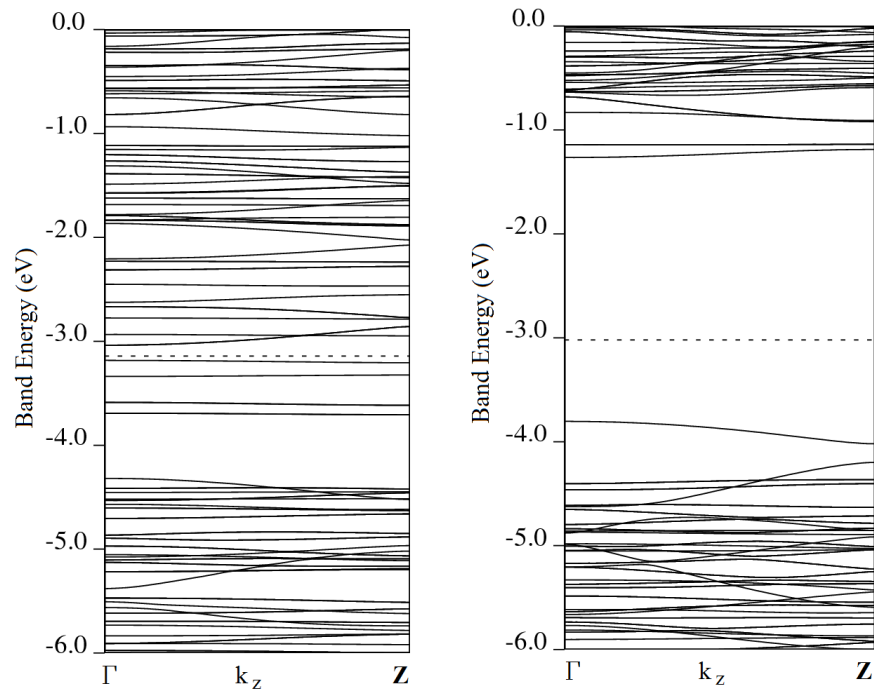


Figure 4.17: Band structures of GaAs/AlAs NWHET(76) and H-GaAs/AlAs NWHET(136) in [111] direction with surface dangling bonds not passivated and passivated with hydrogen-like pseudoatoms, respectively. The surface states are removed from the band gap when the surface dangling bonds have been passivated.

Baldereschi *et al.* [30] have calculated the xy planar averaged potential by taking the average in the growth direction to get a curve for the potential which is varying slowly, from where potential shifts have been obtained. The experimental data for the VBO in GaAs/AlAs range from 0.40 eV to 0.55 eV [65]. Baldereschi *et al.* [30] have calculated the offset for (100), (110) and (111) interfaces in between 0.49-0.51 eV, which is within the experimental error bar.

The 6+6 superlattice is sufficient to obtain band offset values. Since planes parallel to the interface are periodic we have obtained planar averages of charge density and the corresponding electrostatic potential as a function of the direction perpendicular to the interface, which is z coordinate, the growth direction using  $\bar{f}(z) = \frac{1}{S} \int_S f(x, y, z) dx dy$ , where S is the area of the (x, y) plane. So we can have the one dimensional charge density  $\bar{\rho}(z)$  and electrostatic potential  $\bar{V}(z)$  from the three dimensional electronic charge density. If we look at the plot of these planar averages of  $\bar{\rho}(z)$  and  $\bar{V}(z)$  we get periodic functions in GaAs and AlAs materials, smoothly joining across the interface. For the GaAs/AlAs HET system, which is a lattice-matched one, on each side of the interface the period of these periodic functions of  $\bar{\rho}(z)$  and  $\bar{V}(z)$  are the same, which is the half of the bulk lattice parameter. There is a slight difference between these periodic functions due to the effect of the interface which could be enhanced by excluding the bulk-like variations using the macroscopic average technique, which is the one dimensional average of  $\bar{f}$  over a period centered at z:  $\bar{\bar{f}}(z) = \frac{1}{\alpha} \int_{z-\alpha/2}^{z+\alpha/2} \bar{f}(z') dz'$ , where  $\alpha$  is the interplanar distance along the z direction. There is no oscillation on the two part of the interface for the macroscopically averaged quantities as seen in Fig. 4.18, and we get a constant limit in each part of the heterostructure. Therefore, in the interface region deviations are seen from this macroscopic limit. The potential shift can be obtained from this slowly varying curve, as 0.54 eV from this slowly varying curve for the potential, as seen in Fig. 3.5. The valence-band maximum is at  $E_v[GaAs]=5.4127$  eV in the bulk GaAs and  $E_v[AlAs]=5.4021$  eV in the bulk AlAs, so the difference is 0.0106 eV. Therefore the net offset is 0.55 eV, which is close to the experimental value [64] of 0.53 eV.

For nanowire superlattices, which consists of successive segments of GaAs and AlAs nanowires, the potential profile is determined by the surface passivation in addition to the discontinuity at the interface. The potential along the axis of nanowire heterostructure depends both on the dipole layer at each GaAs/AlAs NWHET interface and at the surface of the nanowire. The results indicate that nanoscale heterostructures require more detailed treatments relating

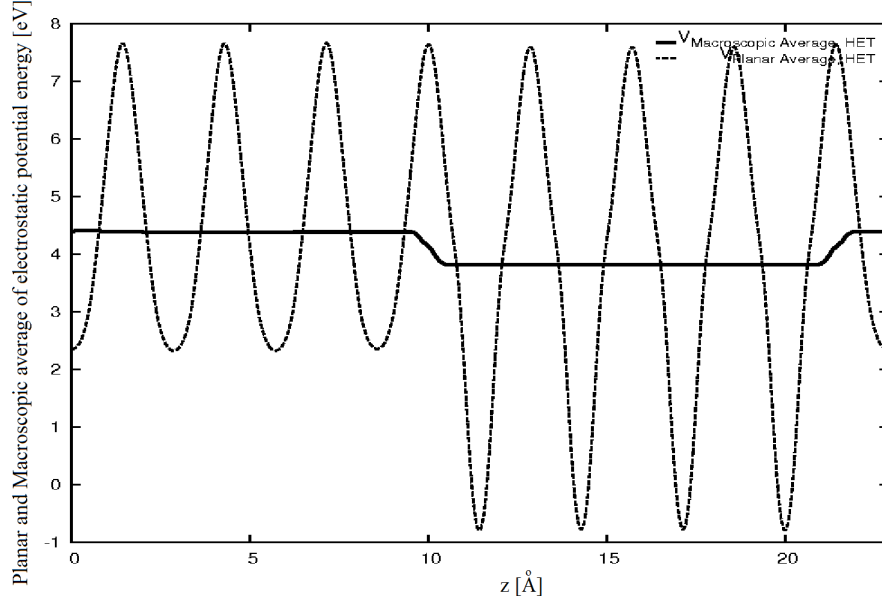


Figure 4.18: For  $(GaAs)_3(AlAs)_3$  superlattices the planar average (dotted line) and macroscopic average (solid line) of electrostatic potential along the growth direction are shown, a steplike behavior is seen. The potential shift corresponds to the difference between the plateaus, which is 0.54 eV in here.

their symmetry, dimensionality and surface passivation. The potential shows the same discontinuity right at the interface also in nanoscale, which is connected to the alignment of the charge-neutrality levels[33, 34] on the different sides of the interface. Therefore, the band offset notion is strong for heterostructures in nanoscale, but the potential lineup is not in a step-like behavior as in the planar bulk heterostructures. The potential profile for 3+3 and 6+6 superlattice GaAs/AlAs NWHET along the [111] direction are calculated. We do not get the constant macroscopic limit on two sides of the nanowire heterostructure, as seen in Fig. 4.19. Although the surfaces have been passivated, the potential has a complex behavior far from the interface, where it is controlled by the surface dipoles. Hence, the inhomogeneous surface termination results in the fluctuating potential which could trap the carriers in the surface. This means that it is possible to control the electronic properties of such axial nanoscale heterostructures with different surface passivations, which may lead to new possibilities for future nanoscale devices.

Niquet *et al.* [10] computed band offsets in core/shell and axial GaAs/AlAs nanowire superlattices with radius 5 nm and 75000 atoms, using self-consistent tight-binding calculations

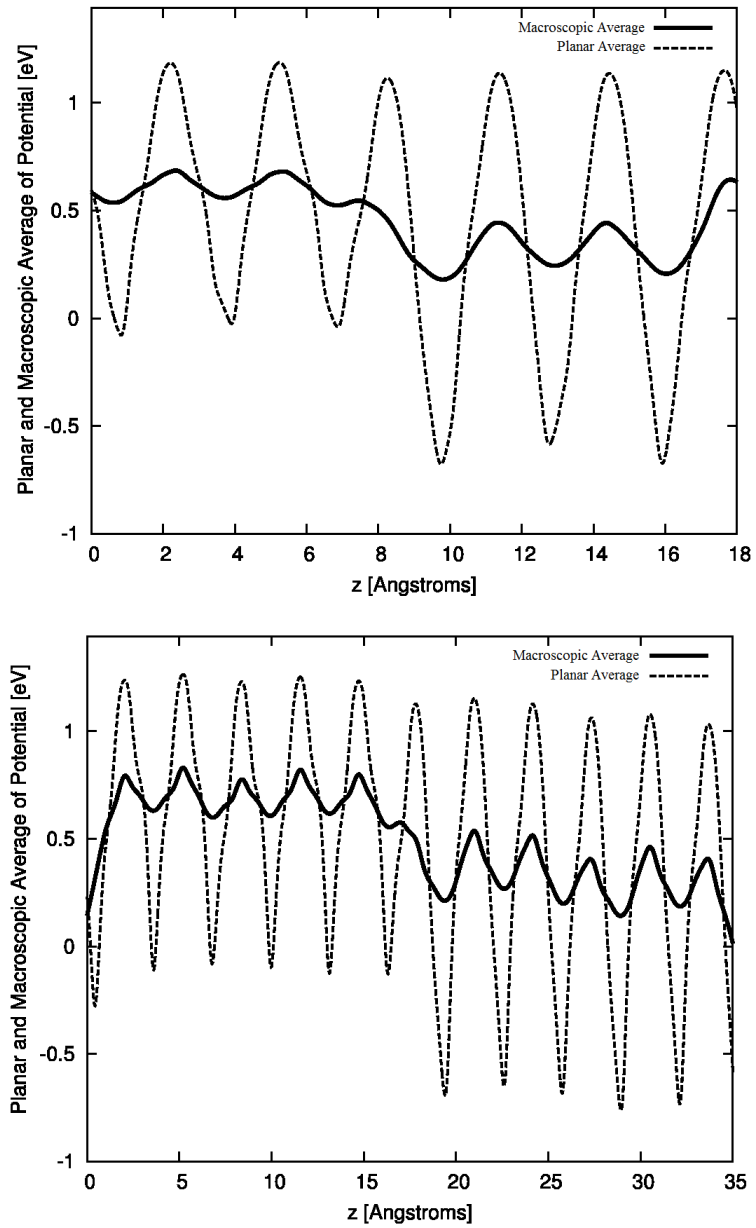


Figure 4.19: The planar (dotted line) and macroscopic (solid line) average of electrostatic potential for the GaAs/AlAs NWHT in the [111] direction with different number of atom supercells, i.e. alternating slabs of GaAs and AlAs are increased. The potential profile for 3+3 and 6+6 superlattice are shown, respectively.



and found that for the nanoscale heterostructures, the band discontinuity at the interface is nearly independent of the size and shape, but the band edges not exactly behaving as a simple step function beyond the interface as in the planar case. They stated that the universally accepted picture for the potential behavior in planar lattice-matched heterostructures, which is constant away from the interface and there is a step at the interface, could be invalid in nanoscale heterostructure. Their results indicated that the band edges can exhibit important oscillations away from the interfaces unless the nanostructures are surrounded with a shell which is homogeneous, that is, in nanowire heterostructures with axial configuration the band edges have a more complicated manner depending on the nature of the surfaces. They have also computed the band offset of nanowires with an external AIAs shell and illustrated the necessity of the surface termination, such that, with this AIAs shell the valence band edge is constant everywhere except at the interface. Leonard and Tersoff [13] found that when a semiconductor carbon nanotube is contacted to a metal, the Schottky barrier height can't be fixed by Fermi level pinning as in semiconductor-metal junctions, that is the behavior is completely different. The summary of finding up to now is that, applications of the concepts of band offsets, driven from the planar heterostructure systems, to nanoscale heterostructure systems is debatable.[10, 13] Recent experiments [12, 66] represent that the nature of the surface capping in nanocrystals determines the energy levels alignment, that is, tuning the ionization potential of nanocrystals is possible.

#### **4.5 Surface dangling-bond states in H-passivated GaAs/AIAs NWHETs**

Defining the valence band offset with energies of valence band edges on both sides of the heterostructure is possible, which can be done by defining a common energy level as a reference for both sides of the heterostructure. The reference level approach is made up of assuming that common energy reference is the same on both side of the interface. Theoretically, lots of such common energy level methods have been suggested. Tersoff's theory of effective midgap states [24] predict band lineups with an error of 0.2 eV. In this section, we report a first-principles study of the electronic properties of surface dangling-bond (SDB) states in hydrogen passivated GaAs/AIAs NWHETs with a diameter of 1 nm. The SDB is defined as the defect due to an non-passivated surface atom.

Van de Walle *et al.* [35] established an important correlation between the location of hy-

hydrogen charge transition levels  $\varepsilon(+/-)$ , which is the Fermi level position where the negative and positive charge states of hydrogen have the same energies, and the band structures of the corresponding materials. They have found a universal alignment of the electrochemical level for the change of positive and negative charge states of hydrogen for a wide variety of materials, that is, hydrogen bond energies are almost the same. The main feature in determining the transition-point energy is the dangling bond state. The positive charge state of hydrogen  $H^+$  binds to the anion and leaves a dangling bond on the neighboring cation. Similarly, the negative charge state of hydrogen  $H^-$  binds to the cation in the material and a dangling bond is created in the neighboring anion. When  $H^+$  binds to the anion, anion atom gives up an electron or the dangling bond gets an electron. This fixes an average of the energies for adding or removing an electron, which is the transition energy at the mid-gap position. Using this mid-gap states it is possible to determine band line-ups of electronic band structures at heterostructures. Remarkably, Van de Walle *et al.* [35] have shown that transition level energies are almost the same for lots of materials, including semiconductors and insulators.

Kagimura *et al.* [36] found that the charge transition levels  $\varepsilon(+/-)$  of SDB states serve like a common energy reference level among Si and Ge wires and Ge/Si heterostructures and they have used this level to predict band line-ups in nanowire heterostructures. They have also stated that charge transition level  $\varepsilon(+/-)$  value for group III and V atoms is constant and a periodic table property. Due to Janak's theorem [67],  $\varepsilon_i = \frac{\partial E}{\partial n_i}$ , SDB's Kohn-Sham eigenvalue is a good approximation for the transition level energy, which is valid if SDB eigenvalue  $\varepsilon_i$  lies within the band gap.

For GaAs/AlAs NWHETs two separate calculations have been carried out for SDB's in this system. The first calculation is performed by removing an hydrogen atom from the surface of GaAs nanowire, specifically from a Ga atom on the surface of the wire. And a second separate calculation is performed for AlAs nanowire by removing a hydrogen atom from an Al atom on the surface of AlAs nanowire. The dangling bond is chosen far away from the GaAs/AlAs nanowire interface. There is a clear resemblance is present in the band structures of the nanowires as seen in Fig. 4.20 . For GaAs and AlAs nanowires  $\varepsilon(+/-)$  lies within the bandgap. Assuming that the hydrogen  $\varepsilon(+/-)$  level occurs at the same "absolute" energy for GaAs and AlAs nanowires, its position at  $E_{VBM} + 1.32eV$  in GaAs and  $E_{VBM} + 1.56eV$  in AlAs. Hence, VBO in GaAs/AlAs heterostructure nanowire system along [111] direction is 0.24 eV.

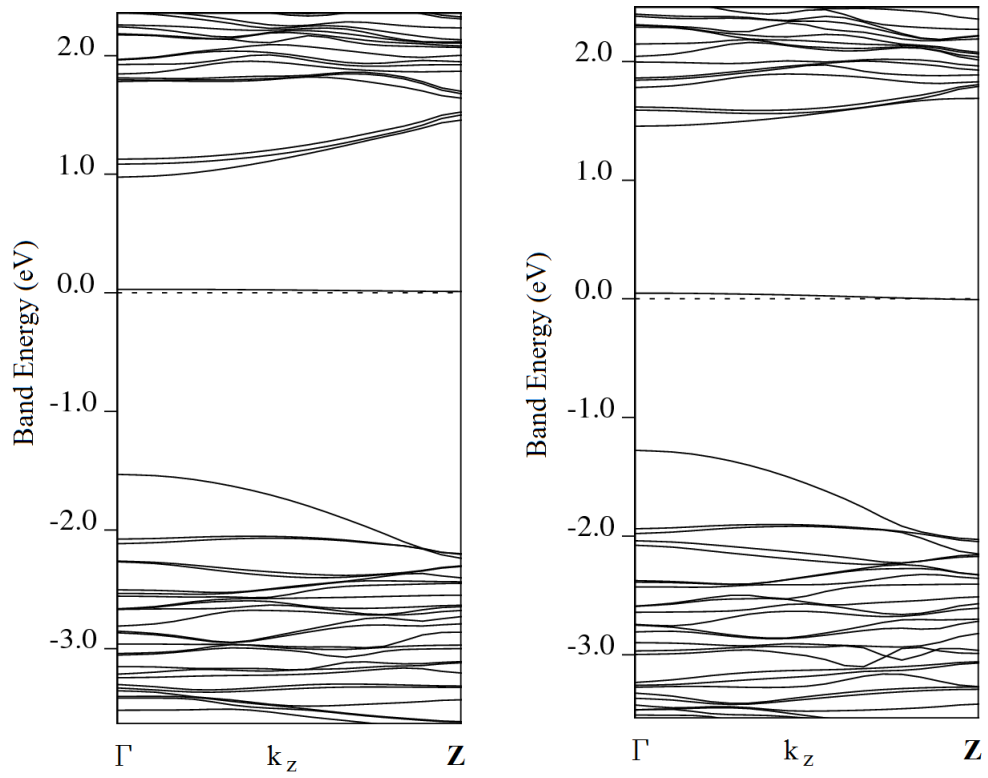


Figure 4.20: Band structures of AlAs and GaAs nanowires with one surface dangling-bond defect, on the left and right side, respectively. Orientation of the wires are along the [111] direction.

## 4.6 Summary

We have shown that, for heterostructures in nanoscale, the potential lineup is not in a step-like behavior as in the planar bulk heterostructures. The potential along the axis of nanowire heterostructure depends both on the dipole layer at each GaAs/AlAs NWHET interface and at the surface of the nanowire. The potential profile for 3+3 and 6+6 superlattice GaAs/AlAs NWHET along the [111] direction are calculated. We do not get the constant macroscopic limit on two sides of the nanowire heterostructure. Because of the nature of the surfaces the potential has a more complex manner far from the interface. Hence the fluctuations in potential far from the interface are developed by the inhomogeneous surface termination. The results indicate that nanowire heterostructures demand more detailed treatments relating their symmetry, dimensionality and surface passivation. Applications of the concepts of band offsets, driven from the planar heterostructure systems, to nanoscale heterostructure systems is debatable.[10, 13] For the nanoscale heterostructures, the fluctuations seen in the potential profile beyond the interface depend on the dispersion of surface dipoles, which control the value of the nanowire potential. We can arrange the inner potential by changing the surface passivation. This means that it is possible to control the electronic properties of axial nanoscale heterostructures with different surface passivations, which may lead to new possibilities for future nanoscale devices.

We report a first-principle calculations of the electronic properties of surface dangling-bond (SDB) states in H passivated GaAs/AlAs NWHETs with a diameter of 1 nm, where the SDB is defined as the defect due to an incomplete passivation of a surface atom. By defining a common energy reference level on each side of the interface it is possible to find the band lineup with energies of band edges on both side of the heterostructure. Theoretically lots of common energy reference level methods have been suggested, such as Tersoff's theory of effective midgap states [24]. The charge transition levels  $\varepsilon(+/-)$  of SDB states serve as a common energy reference level, such that charge transition level  $\varepsilon(+/-)$  value for group III and V atoms is constant. Due to Janak's theorem [67],  $\varepsilon_i = \frac{\partial E}{\partial n_i}$ , SDB's Kohn-Sham eigenvalue is a good approximation for the transition level energy, which is valid if SDB eigenvalue  $\varepsilon_i$  lies within the band gap. For GaAs and AlAs nanowires  $\varepsilon(+/-)$  lies within the bandgap.

## CHAPTER 5

### ALUMINUM NANOWIRES

We have performed first-principles electronic structure calculations of aluminum nanowires for a series of different diameters ranging from 3Å-10Å, which is cut out from a slab of ideal bulk structure along the [001] direction. First-principles calculations of aluminum nanowires have been performed within the density-functional theory. We use the norm-conserving pseudopotentials that are shown to yield successful results for ultrathin nanowire regime. Our results show that the number of bands crossing the Fermi level decreases with decreasing wire diameter and all wires studied are metallic.

Metal nanowires have attracted a vast amount of interest in last years because of their stable structures presenting themselves in a variety of different cross sections. They have been created by mechanically controllable break junction (MCBJ) and scanning tunneling microscopy (STM) and studied both experimentally and theoretically.[68, 69, 70, 71, 72, 73, 74] A variety of regular atomic structures in a variety of sizes have been a great concern in the search of nanodevices.

Gulseren *et al.* [68] studied Al and Pb noncrystalline nanowire structures which are described by empirical many-body inter-atomic "glue" type potentials [75] and they have lead the way for future *ab initio* studies of ultrathin metal wires. They have observed that once the diameter of these metallic wires decreases below a critical value, which is of the order of a few atomic spacings, they develop noncrystalline stable atomic structures which are governed by icosahedral packings of a variety of new structures. Sen *et al.* [69] used first-principles density functional calculations with ultrasoft Vanderbilt-type pseudopotentials[76] using generalized gradient approximation[77] (GGA) for fully relaxed atomic structures and revealed that aluminum can form zigzag and ladder chain structures in planar. In a different study Sen

*et al.* [70] have performed a first-principles study in variety of pentagonal structures within the density functional theory with ultrasoft pseudopotentials using GGA, including pentagonal aluminum nanowires and they have showed that those quasi-one-dimensional pentagonal nanowires comparing to other one-dimensional structures have higher cohesive energies. Using the first principle calculations F. Di Tolla *et al.* [71] studied ultrathin monoatomic, triangular, pentagonal staggered and hexagonal eclipsed Al nanowires, which were obtained from the glue modeling of Al wire in Gulseren *et al.* [68] They have found that the smallest crystalline fcc wires are the hexagonal wires and they stated that glue models are not adequately accurate for ultrathin wires and further *ab initio* improvement is needed. Structures and electronic properties of stable coaxial and helical aluminum nanowires [72] are also studied using the first-principle calculations with density functional theory and with norm-conserving pseudopotentials using GGA method by Perdew-Wang 1991 (PW91) functional.[78] For the metallic nanowires it was shown that there is a noncrystalline-crystalline transition depending on the size, that is below a critical radius the most stable structures are in helical packing and for larger radius than this critical value the wire favored the fcc structure depending on the metallic element used in the nanowire.[68, 73, 74]

This chapter presents a first-principles analysis of very thin Al nanowires, which is cut out from a slab of ideal bulk structure of aluminum along the [001] direction. In order to study the size dependence of the electronic structure we consider four different wires with increasing radii and cross-sections, namely: wires with radius  $3\text{\AA}(4)$ ,  $5\text{\AA}(16)$ ,  $7\text{\AA}(32)$  and  $10\text{\AA}(76)$ , where  $r\text{\AA}(N)$  shows radius and number of atoms in the supercell, as shown in Fig. 5.1. It is found that Al nanowires below  $3\text{\AA}$  are of helical structure and as  $r > 3\text{\AA}$  the nanowire structures have the multi-walled cylindrical form, which consists of closed-packed curved layers as seen in Fig. 5.1. As  $r > 10\text{\AA}$  in the core region of the nanowire, the crystalline fcc structures are formed.[68, 73, 74] We also find that the number of bands crossing the Fermi level decreases with decreasing wire diameter and all wires studied in this chapter are metallic. We use the norm-conserving pseudopotentials that are shown to yield successful results for ultrathin nanowire regime, that is for planar atomic wires and pentagonal wires.[70, 69]

## 5.1 Method and Atomic Structure

In this chapter first-principles plane wave calculations are carried out for straight nanowires within the supercell geometry. Aluminum nanowires are periodic along the growth direction, which is the z-direction, and all of them are periodically repeated as a parallelepiped lattice with a sufficient spacing in the x-y plane to reduce the interaction between one wire and its periodic image. Our calculations are based on the first-principles density functional theory (DFT), which are carried out using PWscf package program [22]. We use the generalized gradient approximation (GGA) method [77] by Perdew-Burke-Erzerhof (PBE) functional [79] for the exchange-correlation and norm-conserving pseudopotentials determined by the Hamann method [80] to obtain electronic structure and total energy of relaxed aluminum nanowires.

For the metallic nanowire system, the atomic positions were allowed to relax for atoms to find their minimum energy configuration. For the calculations relating the Al nanowire system in the [001] crystallographic direction we use a 50 Ry energy cutoff. Brillouin zone sampling is performed using a [1X1X50] Monkhorst-Pack grid [54] and Brillouin zone integration is performed using the Methfessel-Paxton smearing method [62] with a smearing width of 10mRy. The convergence tests for the energy cutoff value and the number of k points are done. All the calculations have been carried out with atoms in their fully relaxed positions.

## 5.2 Results and Discussions

The relaxed aluminum nanowires studied in this paper are shown in Fig. 5.1, in which there are four different wires with increasing radii and cross-sections, namely: wires with radius  $3\text{\AA}$ (4),  $5\text{\AA}$ (16),  $7\text{\AA}$ (32) and  $10\text{\AA}$ (76), where  $r\text{\AA}$ (N) shows radius and number of atoms in the supercell. In Fig.1a, the radius of the wire is taken as  $3\text{\AA}$  with 4 atoms in the supercell and top and side views are shown. In the same way, in Fig.1b, 1c and 1d, the top and side views of the wires with radius  $5\text{\AA}$  with 16 atoms in the supercell,  $7\text{\AA}$  with 32 atoms in the supercell and  $10\text{\AA}$  with 76 atoms in the supercell are shown, respectively. The lattice constant of the Al nanowire which minimizes the total energy is shown in Table 5.1 for all nanowires studied in this chapter, which are rather close to the bulk lattice constant  $a_{fcc} = 7.67\text{a.u.}$  of aluminum.

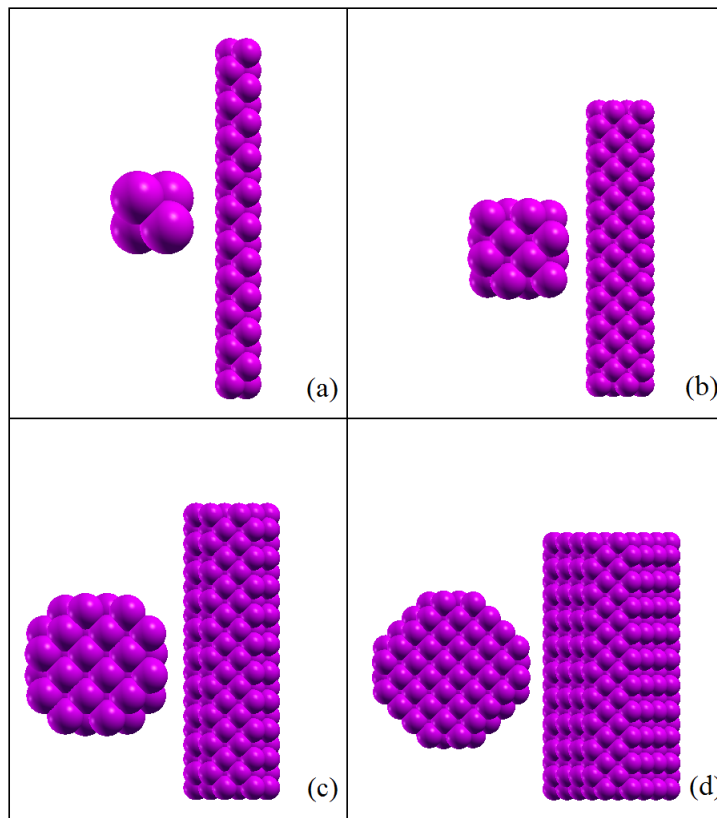


Figure 5.1: Top and side views of aluminum nanowires with radius (a)  $3\text{\AA}$ (4), (b)  $5\text{\AA}$ (16), (c)  $7\text{\AA}$ (32) and (d)  $10\text{\AA}$ (76).

Table 5.1: Aluminum nanowire lattice constant along the wire axis.

Type	Lattice constant (a.u.)
AlNW(4)	7.56
AlNW(16)	7.58
AlNW(32)	7.69
AlNW(76)	7.59



In order to understand the material behavior of the stable geometries of nanowires we performed electronic band structure analysis. In Fig. 5.2 band structures of Al nanowires studied are shown. It is seen in the band structure for the wire with radius 3Å that the bands are quite broad and the wire is metallic, which is shown in Fig. 5.2a. Similarly, In Fig.5.2b, 5.2c and 5.2d, the band structure for the wires with radius 5Å, 7Å and 10Å are shown, respectively. It is observed that the forms of energy band structures are similar, but the number of energy bands crossing the Fermi level is different, which is important for the stability and quantum ballistic conductance of nanowire. Under ideal conditions, in order to determine the conductance the number of bands crossing the Fermi level is counted. It is observed that the number of bands crossing the Fermi level decreases with decreasing wire diameter and also all wires studied are metallic. The bands are mainly extended. We do not notice any strong localization due to bonding.

The nature of the bonding in these aluminum nanowire structures is searched out by the electronic charge density contour plots in the lateral and vertical planes, which are shown in Fig. 5.3 for 3Å(4), 5Å(16), 7Å(32) and 10Å(76), respectively. Left panels show the charge density contours in lateral planes and right panels show the charge density contours in vertical planes. The charge distribution in vertical plane has a directional character in most cases, since in one dimensional structures of Al bonding attains directionality. It is observed that charge is concentrated between atoms constituting a directional bond.

The cohesive energy (per Al atom) of AlNWs is calculated by

$$E_c = E_T[Al] - \frac{E_T[AlNW(N)]}{N} \quad (5.1)$$

using the total energy of free Al atom and the Al nanowire's total energy having N atoms AlNW(N) and having optimized structure shown in Table 5.2 which are calculated for different diameters. Calculated cohesive energies show that among the wires we analyzed the wire with a radius of 7(Å) AlNW(32) is the most stable, with the highest binding energy.

### 5.3 Summary

We have studied four different ultrathin aluminum nanowires which are cut out from a slab of ideal bulk structure along the [001] direction based on density functional formalism with norm-conserving pseudopotentials that are shown to yield successful results for ultrathin

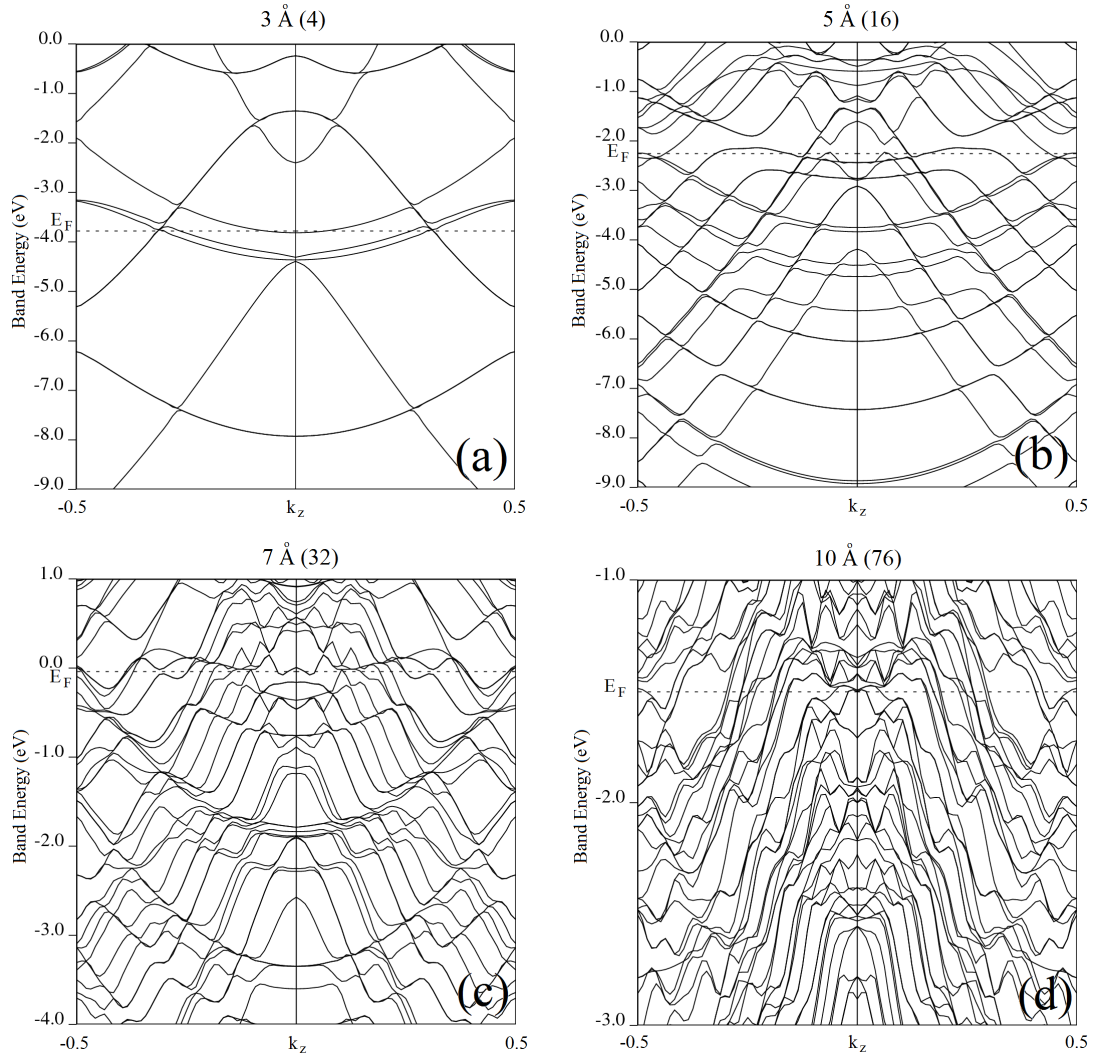


Figure 5.2: Band structures of Al nanowires with radius (a) 3Å(4), (b) 5Å(16), (c) 7Å(32) and (d) 10Å(76)

Table 5.2: Cohesive energy per Al atom pair  $E_c$  of different radius Al nanowires calculated using Eq. (1).

Type	$E_c$ (eV)	Total Energy (eV)
AlNW(4)	2.28	-220.40
AlNW(16)	3.01	-893.25
AlNW(32)	3.18	-1792.06
AlNW(76)	2.86	-4232.01

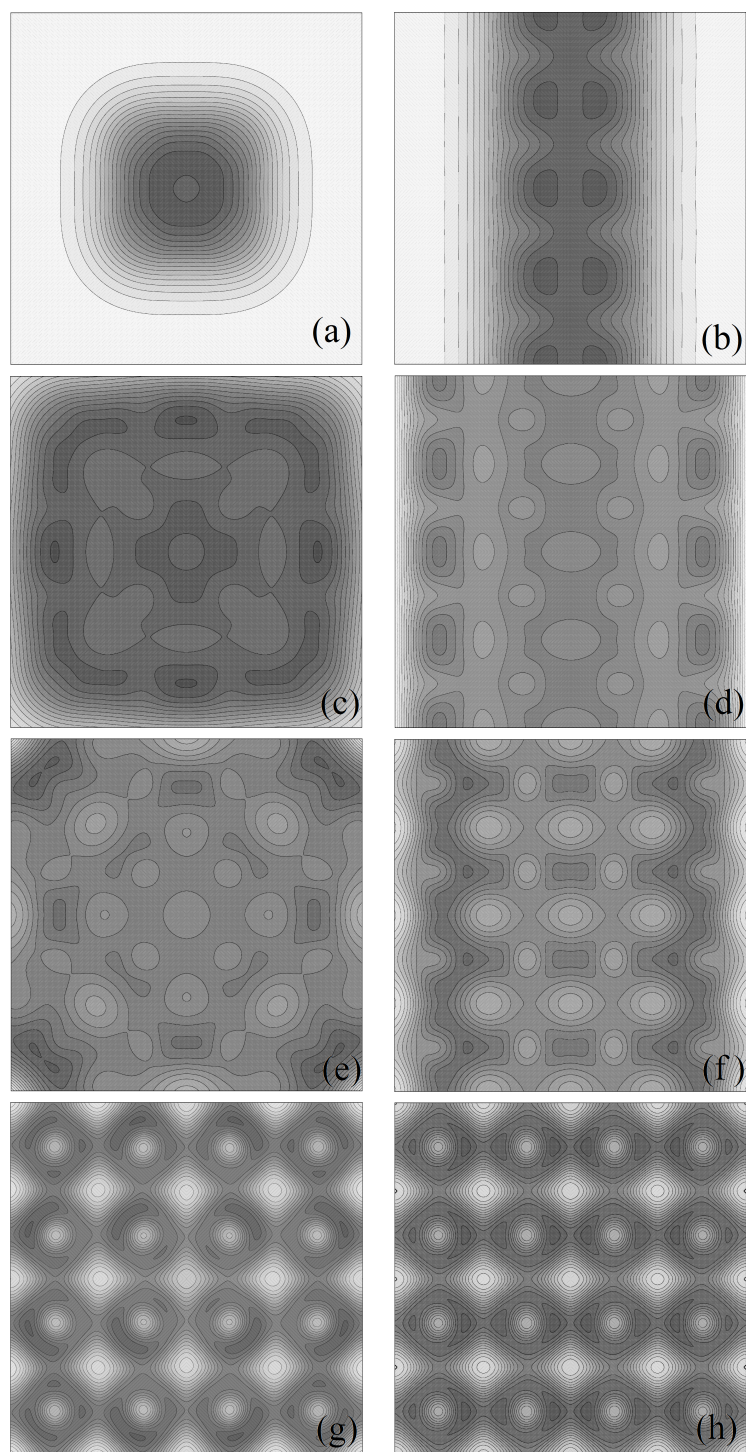


Figure 5.3: Charge density contour plots in lateral and vertical planes are shown in left panels and right panels, respectively. (a) and (b):  $3\text{\AA}(4)$ . (c) and (d):  $5\text{\AA}(16)$ . (e) and (f):  $7\text{\AA}(32)$ . (g) and (h):  $10\text{\AA}(76)$ .

nanowire regime. We have found that Al nanowires below  $3\text{\AA}$  are of helical structure and as  $r > 3\text{\AA}$  the nanowire structures have the multi-walled cylindrical form, and as  $r > 10\text{\AA}$  in the core region of the nanowire, the crystalline fcc structures are formed. We have also found that the number of bands crossing the Fermi level decreases with decreasing wire diameter and all wires investigated in this thesis are metallic. The bands are mainly extended. We do not notice any strong localization due to bonding. Since in one dimensional structures of Al bonding attains directionality the calculated charge distributions in vertical planes have a directional character.

## CHAPTER 6

### CONCLUSION

We used first-principles plane-wave calculations within the density functional theory with the localized density approximation (LDA) to get information about the structural and electronic properties of bare and hydrogen passivated GaAs/AlAs nanowire heterostructures. All nanowires studied were constructed by selecting an axis along a crystallographic direction in bulk zinc blende and taking the atoms which are in a chosen distance from the nanowire axis. We studied for the effects of the surface passivation on the band gap and the band offsets for the planar GaAs/AlAs bulk heterostructure system and GaAs/AlAs nanowire heterostructure system and showed that the properties of bare and H-GaAs/AlAs NWHETs are quite different.

The dangling bond states on the surface of a semiconductor in nanoscale are electronically active states. Surface passivation with some passivation agent is needed without harming the neutrality of the system. Aim of the surface passivation is cleaning the band gap from the localized surface states [63]. We have used a fictitious hydrogen as a passivation agent. We showed that surface passivation has cleared the band gap from the localized surface states.

The determination of band offsets at interfaces of heterostructures is a requirement for semiconductor device design since, by controlling the band offsets, we can control the charge carrier flow and confinement. It is possible to control the potential that carriers feel in semiconductor heterostructures. For the planar bulk lattice-matched heterostructures, the macroscopic average of potential of the two materials is constant far from the interface and there is a discontinuity at the interface depending on the composition of the heterostructure. In order to obtain the valence band offset in the bulk heterostructure system, the shift in the macroscopic potential at the interface and the difference between the valence band maximum values of the two constituents must be added. In nanoscale heterostructures, the potential profile presents

a more complex picture. The results indicate that while the discontinuity remains close to the planar limit right at the interface, there are fluctuations on the average potential profile beyond the interface developed by the inhomogeneous surface termination, that is, there are oscillations of the band edges away from the interface. The summary of finding up to now is that, applications of the concepts of band offsets, driven from the planar heterostructure systems, to nanoscale heterostructure systems is debatable.[10, 13] We have showed that the universally accepted picture for the potential behavior in planar lattice-matched heterostructures, which is constant away from the interface and there is a step at the interface, is invalid in nanoscale heterostructure.

For nanowire superlattices, which consists of successive segments of GaAs and AlAs nanowires, the potential profile is determined by the surface passivation in addition to the discontinuity at the interface. The potential along the axis of nanowire heterostructure depends both on the dipole layer at each GaAs/AlAs NWHET interface and at the surface of the nanowire. The results indicate that nanowire heterostructures demand more detailed treatments relating their symmetry, dimensionality and surface passivation. Because of the nature of the surfaces the potential has a more complex manner far from the interface. Hence the fluctuations in potential far from the interface are developed by the inhomogeneous surface termination. This means that, it is possible to control the electronic properties of such axial nanoscale heterostructures with different surface passivations, which may lead to new possibilities for future nanoscale devices.

We have shown that, for heterostructures in nanoscale, the potential lineup is not in a step-like behavior as in the planar bulk heterostructures. The potential along the axis of nanowire heterostructure depends both on the dipole layer at each GaAs/AlAs NWHET interface and at the surface of the nanowire. The potential profile for 3+3 and 6+6 superlattice GaAs/AlAs NWHET along the [111] direction are calculated. We do not get the constant macroscopic limit on two sides of the nanowire heterostructure. For the nanoscale heterostructures, the fluctuations seen in the potential profile beyond the interface depend on the dispersion of surface dipoles, which control the value of the nanowire inside potential. This means that, we can arrange the inner potential by changing the surface passivation.

Defining the valence band offset with energies of valence band edges on both sides of the heterostructure is possible, which can be done by defining a common energy level as a reference

for both sides of the heterostructure. We report a first-principles study of the electronic properties of surface dangling-bond (SDB) states in hydrogen passivated GaAs/AlAs NWHETs with a diameter of 1 nm. There is an important correlation between the location of hydrogen charge transition levels  $\varepsilon(+/-)$ , which is the Fermi level position where the negative and positive charge states of hydrogen have the same energies, and the band structures of the corresponding materials. Van de Walle *et al.* [35] have shown that transition level energies are almost the same for a wide range of materials. The charge transition levels  $\varepsilon(+/-)$  of SDB states serve as a common energy reference level, such that charge transition level  $\varepsilon(+/-)$  value for group III and V atoms constant. We report a first-principles study of the electronic properties of surface dangling-bond (SDB) states in hydrogen passivated GaAs/AlAs NWHETs with a diameter of 1 nm, where the SDB is defined as the defect due to an incomplete passivation of a surface atom. By defining a common energy reference level on each side of the interface it is possible to find the band lineup with energies of the valence band edges on both sides of the heterostructure as proposed in Tersoff's theory of effective midgap states [24]. For GaAs/AlAs NWHETs two separate calculations have been carried out for SDB's in this system. The first calculation is performed by removing an hydrogen atom from the surface of GaAs nanowire, specifically from a Ga atom on the surface of the wire. And a second separate calculation is performed for AlAs nanowire by removing a hydrogen atom from an Al atom on the surface of AlAs nanowire. The dangling bond is chosen far away from the GaAs/AlAs nanowire interface. Striking resemblance in both band structures were shown. For GaAs and AlAs nanowires  $\varepsilon(+/-)$  lies within the bandgap.

We have also studied four different ultrathin aluminum nanowires which are cut out from a slab of ideal bulk structure along the [001] direction based on density functional formalism with norm-conserving pseudopotentials that are shown to yield successful results for ultrathin nanowire regime. We have found that Al nanowires below  $3\text{\AA}$  are of helical structure and as  $r > 3\text{\AA}$  the nanowire structures have the multi-walled cylindrical form, and as  $r > 10\text{\AA}$  in the core region of the nanowire, the crystalline fcc structures are formed. We have also found that the number of bands crossing the Fermi level decreases with decreasing wire diameter and all wires investigated in this thesis are metallic. The bands are mainly extended. We do not notice any strong localization due to bonding. Since in one dimensional structures of Al bonding attains directionality the calculated charge distributions in vertical planes have a directional character.

## REFERENCES

- [1] M. T. Bjork, B. J. Ohlsson, C. Thelander, A. I. Persson, K. Deppert, L. R. Wallenberg, and L. Samuelson, *Appl. Phys. Lett.* **81**, 4458 (2002).
- [2] E. Lind, A. I. Persson, L. Samuelson, and L.-E. Wernersson, *Nano Lett.* **6**, 1842 (2006).
- [3] C. Thelander, T. Matensson, M. T. Bjork, B. J. Ohlsson, M. W. Larsson, L. R. Wallenberg, and L. Samuelson, *Appl. Phys. Lett.* **83**, 2052 (2003).
- [4] M. T. Bjork, A. Fuhrer, A. E. Hansen, M. W. Larsson, L. E. Froberg, and L. Samuelson, *Phys. Rev. B* **72**, 201307(R) (2005).
- [5] A. Fuhrer, L. E. Froberg, J.N. Pedersen, M. W. Larsson, A. Wacker, M.-E. Pistol, and L. Samuelson, *Nano Lett.* **7**, 243 (2007).
- [6] C. Thelander, H. A. Nilsson, L. E. Jensen, and L. Samuelson, *Nano Lett.* **5**, 635 (2005) .
- [7] H. A. Nilsson, C. Thelander, L. E. Froberg, J. B. Wagner, and L. Samuelson, *Appl. Phys. Lett.* **89** (2006) 163101.
- [8] M. P. Persson and H. Q. Xu, *Phys. Rev. B* **73**, 035238 (2006).
- [9] Jie Xiang, Wei Lu, Yongjie Hu, Yue Wu, Hao Yan, Charles M. Lieber, *Nature* **441**, 04796 (2006).
- [10] Y. M. Niquet and C. Delerue, *Phys. Rev. B* **84**, 075478 (2011).
- [11] Xiaocheng Jiang, Qihua Xiong, *Nano Lett.*, **7**, 3214 (2007).
- [12] M. Soreni-Harari, N. Yaacobi-Gross, D. Steiner, A. Aharoni, U. Banin, O. Millo, and N. Tessler, *Nano Lett.*, **8**, 678 (2008).
- [13] F. Leonard and J. Tersoff, *Phys. Rev. Lett.* **84**, 4693 (2000).
- [14] X. Zhao, C. M. Wei, L. Yang, and M. Y. Chou, *Phys. Rev. Lett.* **92**, 236805 (2004).
- [15] Y. Zheng, C. Rivas, R. Lake, K. Alam, T. B. Boykin, and G. Klimeck, *IEEE Trans. Electron Devices* **52**, 1097 (2005).
- [16] J. Li and A. J. Freeman, *Phys. Rev. B* **74**, 075333 (2006).
- [17] R. Kagimura, R. W. Nunes, and H. Chacham, *Phys. Rev. Lett.* **98**, 026801 (2007).
- [18] R. Rurali and N. Lorente, *Phys. Rev. Lett.* **9**, 026805 (2005).
- [19] W. Fan, H. Xu, A. L. Rosa, T. Frauenheim, and R. Q. Zhang, *Phys. Rev. B* **76**, 073302 (2007).
- [20] S. Cahangirov and S. Ciraci, *Phys. Rev. B* **79**, 165118 (2009).



- [21] D. Vanderbilt, Phys. Rev. B **41**, 7892 (1990).
- [22] S. Baroni, A. Dal Corso, S. de Gironcoli, P. Giannozzi, (<http://www.pwscf.org>).
- [23] Anderson R L IBM J. Res. Dev. **4**, 283 (1960).
- [24] Tersoff J Phys. Rev. B **30**, 4874 (1984).
- [25] Bass J M, Oloumi M and Matthai C C J. Phys.: Condens. Matter **1**, 10625 (1989).
- [26] Lambercht W R L and Segall B Phys. Rev. Lett. **61**, 1764 (1988).
- [27] Lambercht W R L and Segall B and Anderson O K Phys. Rev B **41**, 2813 (1990).
- [28] Bylander D M and Kleinman L Phys. Rev B **36**, 3229 (1987).
- [29] Bylander D M and Kleinman L Phys. Rev. Lett. **59**, 2091 (1987).
- [30] Baldereschi A, Baroni S and Resta R Phys. Rev. Lett. **61**, 734 (1988).
- [31] Zhang X H, Chua S J, Xu S J and Fan W J J. Phys.: Condens. Matter **10**, 577 (1988).
- [32] Wei S-H and Zunger A Appl. Phys. Lett. **72**, 2011 (1998).
- [33] F. Flores and C. Tejedor, J.Phys. C **20**, 145 (1987).
- [34] J. Tersoff, Phys. Rev. Lett. **52**, 465 (1984).
- [35] C. G. Van de Walle and J. Neugebauer, Nature (London) **423**, 626 (2003).
- [36] R. Kagimura, R. W. Nunes, and H. Chacham, Phys. Rev. Lett. **98**, 026801 (2007).
- [37] M. Born and J. R. Oppenheimer, Ann. der Phys. **84**, 457 (1927).
- [38] D. R. Hartree, Proc. Cambridge. Philos. Soc. **24**, 89 (1928).
- [39] V. Fock, Z. Phys. **61**, 126 (1930).
- [40] J. C. Slater, Phys. Rev. **35**, 210 (1930).
- [41] L. H. Thomas, Proc. Cambridge. Philos. Soc. **23**, 542 (1927).
- [42] E. Fermi, Z. Phys. **48**, **73** (1928).
- [43] P. Hohenberg and W. Kohn, Phys. Rev. **136**, B864 (1964).
- [44] W. Kohn and L. J. Sham, Phys. Rev. **140**, A1133 (1965).
- [45] J.P. Perdew and A. Zunger, Phys. Rev. B **23**, 5048 (1981).
- [46] D.M. Ceperley and B.J. Alder, Phys. Rev. Lett. **45**, 566 (1980).
- [47] J. P. Perdew and Y. Wang, Phys. Rev. B, **45**, 13244 (1991).
- [48] A. D. Becke, Phys. Rev. A **38**, 3098-3100 (1988).
- [49] C. Lee, W. Yang and R. G. Parr, Phys. Rev. B **37**, 785 (1988).
- [50] J.P. Perdew, K. Burke, and M. Ernzerhof, Phys. Rev. Lett. **77**, 3865 (1996).

- [51] C. Kittel *Introduction to Solid State Physics* Wiley and Sons, New York, (1996).
- [52] A. Baldereschi *Phys. Rev. B* **12**, 5212 (1973).
- [53] D. J. Chadi and M. L. Cohen *Phys. Rev. B* **8**, 4547 (1973).
- [54] H.J. Monkhorst and J. P. Pack *Phys. Rev. B* **13**, 5188 (1976).
- [55] S. Froyen *Phys. Rev. B* **39**, 3168 (1989).
- [56] M. C. Payne, M. P. Teter, D. C. Allan, T. A. Arias, J. D. Joannopoulos, *Rev Mod Phys* **64**, 1045 (1992).
- [57] W. E. Pickett, *Computer Phys. Rep.* **9**, 115 (1989).
- [58] O. H. Nielsen and R. M. Martin, *Phys. Rev. Lett.* **50**, 697 (1983).
- [59] O. H. Nielsen and R. M. Martin, *Phys. Rev. B* **32**, 3780 (1985).
- [60] O. H. Nielsen and R. M. Martin, *Phys. Rev. B* **32**, 3792 (1985).
- [61] A. Kokalj, *Comp. Mat. Sci.* **28**, 155 (2003), [www.xcrysden.org](http://www.xcrysden.org)
- [62] M. Methfessel and A. T. Paxton, *Phys. Rev. B* **40**, 3616 (1989).
- [63] Xiangyang Huang, Eric Lindgren, and James R. Chelikowsky *Phys. Rev. B* **71**, 165328 (2005).
- [64] I. Vurgaftman, J. R. Meyer, and L. R. Ram-Mohan, *J. Appl. Phys.* **89**, 5815 (2001).
- [65] W. I. Wang and F. Stern, *J. Vac. Sci. Technol. B* **3**, 1280 (1985).
- [66] D. Aldakov, F. Chandezon, R. De Bettignies, M. Firon, P. Reiss, and A. Paron, *Eur. Phys. J. Appl. Phys.* **36**, 261 (2006).
- [67] J. F. Janak, *Phys Rev B* **18**, 7165 (1978).
- [68] O. Gulseren, F. Ercolessi, E. Tosatti, *Phys. Rev. Lett.* **80**, 3775 (1998).
- [69] P. Sen, S. Ciraci, A. Buldum, and Inder P. Batra, *Phys. Rev. B* **64**, 195420 (2001).
- [70] P. Sen, O. Gulseren, T. Yildirim, Inder P. Batra, and S. Ciraci, *Phys. Rev. B* **65**, 235433 (2002).
- [71] F. Di Tolla, A. Dal Corso, J. A. Torres, E. Tosatti, *Surface sciences* **454-456**, 947-951 (2000).
- [72] T. Makita, K. Doi, K. Nakamura, and A. Tachibana, *Journal of Chemical Physics* **119**, 538 (2003).
- [73] Y. Kondo and K. Takayanagi, *Phys. Rev. Lett.* **79**, 3455 (1997).
- [74] B. Wang, S. Yin, G. Wang, A. Buldum, and J. Zhao, *Phys. Rev. Lett.* **86**, 2046 (2001).
- [75] F. Ercolessi, E. Tosatti, and M. Parrinello, *Phys. Rev. Lett.* **57**, 719 (1986).
- [76] D. Vanderbilt, *Phys. Rev. B* **41**, 7892 (1990).

- [77] J. P. Perdew, J. A. Chevary, S. H. Vosko, K. A. Jackson, M. R. Pederson, D. J. Singh, and C. Fiolhais, *Phys. Rev. B* **46**, 6671 (1992).
- [78] J. P. Perdew and Y. Wang, *Phys. Rev. B* **45**, 13244 (1992).
- [79] J.P. Perdew, K. Burke, and M. Ernzerhof, *Phys. Rev. Lett.* **77**, 3865 (1996).
- [80] D. R. Hamann, *Phys. Rev. B* **40**, 2980 (1989).

## VITA

Selma Şenozan was born in Konya, Turkey in 1979.

1998-2002 Middle East Technical University, Physics, Advanced Physics Program; Ankara, Turkey.

2002-2005 Middle East Technical University, Physics, The Degree of Master of Science; Ankara, Turkey. *A Continuum Model For Decoherence in 1D Transport*, Supervisor: Assoc. Prof. Dr. Sadi Turgut

2005- She started her Ph.D. studies in Theoretical Solid State Physics at Middle East Technical University, Physics; Ankara, Turkey. *First-Principles study of GaAs/AlAs nanowire heterostructures*, Supervisor: Prof. Dr. Mehmet Tomak

Publications:

1. S. Şenozan, S. Turgut, M. Tomak *A continuum model for dephasing in mesoscopic systems*, Physica E **43** (2011) 1845-1852
2. S. Şenozan and M. Tomak *First principles study of aluminum nanowires*, submitted to Physica E
3. S. Şenozan and M. Tomak *First principles study of GaAs/AlAs nanowire heterostructures*, submitted to Physical Review B